UNIVERSIDAD DE CHILE
FACULTAD DE CIENCIAS FÍSICAS Y MATEMÁTICAS
DEPARTAMENTO DE ASTRONOMÍA

POINT SPREAD FUNCTION SUBTRACTION IN INTEGRAL FIELD SPECTROSCOPY

TESIS PARA OPTAR AL GRADO DE MAGÍSTER EN CIENCIAS, MENCIÓN ASTRONOMÍA

VACHAIL NICOLÁS SALINAS POBLETE

PROFESOR GUÍA:
SIMON CASASSUS MONTERO

PROFESOR CO-GUÍA:
ANDRES JORDAN COLZANI

MIEMBROS DE LA COMISIÓN:
CATHERINE DOUGADOS
MARIO HAMUY WACKENHUT
PATRICIO ROJO RUBKE

SANTIAGO DE CHILE
OCTUBRE 2013

To my beloved mother.

Whose passion for the universe ignited my curiosity.

Acknowledgements

Foremost, I would like to express my sincere gratitude to my advisor Prof. Simon Casassus for the continuous support of my MSc study and research, for his patience, motivation, and enthusiasm.

Besides my advisor, I would like to thank my co-advisor Prof. Andres Jordan, whose help and contribution was fundamental to the whole project.

My sincere thanks also goes to the millennium alma disk nucleus (MAD) and MAD members, who have guide me and contributed to my education.

I thank my fellow classmates: Jose Utreras, Paula Lopez, Elise Servajean, Ricardo Ramirez and Valentin Christiaens for the stimulating discussions, and constant support in this task. Special thanks to Paula Sanchez and Maritza Soto, for the countless weekends we worked together before deadlines, and multiple study sessions.

Also I thank my mother, for her unconditional support, and to my boyfriend, who had to put up with me countless times when work prevent us of being together, and for his unconditional love.

Abstract

Direct Imaging of circumstellar material and forming exoplanets around young stellar objects (YSO's) is a challenging task. Several techniques have been developed for this purpose, among them we focused on the spectral deconvolution technique(SD). Our goal is to create an algorithm that improves the current state of the art of the SD technique, using principal component analysis (PCA) to create an orthogonal basis set in annular regions centred on the star. A selection criterion for the wavelength channels used to estimate the basis set, ensures that the model PSF is minimally contaminated by a possible faint companion. We test our algorithm using SINFONI data of HD 142527, HD 100546 and T Cha, obtaining a high-resolution image of the surrounding disks in the H+K band. l-SDI gets roughly twice the amount of throughput of its non-localized version. Using l-SDI we give new upper limit detection curves on the selected sources, we confirm the structure of HD 142527 in the literature and report a new spiral-arm structure in the outer disk.

La detección directa de material circumestelar y la formación planetaria alrededor de objetos estelares jóvenes (YSO's en ingles) es una tarea compleja. Muchas tecnicas han sido desarrolladas para este propósito, y esta tesis se enfoca en la técnica de deconvolución espectral (SD). El objetivo es crear un algoritmo capaz de mejorar las versiones actuales de SD, mediante el analisis de componentes principales (PCA) para crear un conjunto de bases ortogonales entre si en regiones anulares centradas en la estrella. Un criterio que selecciona los canales de longitud de onda usados para construir esta base, asegura que el modelo de la PSF no este totalmente contaminado por un posible compañero. El algoritmo es puesto a prueba con datos obtenidos en SINFONI de las fuentes HD 142527, HD 100546 y T Cha, obteniendo una imagen de alta resolución de el material circumestelar en la banda H+K. l-SDI obtiene aproximadamente dos veces la cantidad de 'throughput' (rendimiento) que su version no localizada. Usando l-SDI nuevas curvas de limites superiores en detección son extraídas de las fuentes seleccionadas, se confirma la estructura de HD 142527 en la literatura y se reporta un nueva estructura brazo-espiral en el disco exterior.

Contents

List of Figures

Chapter 1

Introduction

The search of outer worlds is a quest that has intrigued humanity for ages. Firstly in our own planet, but lately this search has expanded further into space. Almost 18 years have passed since the first announcement of a Jupiter-sized planet 51 Peg b orbiting a sun-like star[Mayor and Queloz, 1995], and now according to the exoplanet.eu Database Schneider et al. [2012] more than 1000 exoplanets have been found and confirmed using various and sofisticated methods, and the list keeps growing. Most of these detections are made by inderect methods, but a fraction of them are directly detected, i.e. using direct imaging. As the name suggest it, the observation of the companion itself is required to confirm the detection. This implies a high-contrast technique to be used in order to reveal the companion.

This thesis will focus on a direct imaging technique called Spectral Deconvolution and will develope further on its constrains and limits. We understand as contrast, the ratio between the light fulx of a bright source (the host star), and a faint source (the companion). Then we define a high-contrast observation as the techique that reaches a ratio of $\sim 10^4$ of contrast [Oppenheimer and Hinkley, 2009].

Historically, direct imaging of faint companions has been performed using coronographic imaging, and applying sophisticated analysis techniques to identify faint point sources in the speckle noise. Nowadays the techniques for high-contrast imaging make use of angular differential imaging [ADI, Marois et al., 2006], and spectral difference imaging [SDI, e.g. Lenzen et al., 2004; Marois et al., 2005]. A few sophisticated algorithms exists to subtract the point spread function (PSF) of the host star in the observations to reveal faint companions. The LOCI algorithm subtracts the stellar PSF by computing optimal linear combinations of the ADI samples [Lafrenière et al., 2007]. A damped version of LOCI (d-LOCI) was introduced by Pueyo et al. [2012a], and applied to Integral Field Spectrograph (IFS) data [Pueyo et al., 2012b] . A faster ADI algorithm uses Principal Component Analysis (or Karhuenen-Loève Transform) to produce an orthonormal basis for the linear combination representing the PSF using the whole dataset [Amara and Quanz, 2012; Soummer et al., 2012].

``Spectral deconvolution'' is a technique that uses integral field spectroscopy (IFS) data to make an estimate of the stellar PSF in each channel of the cube using the spectral variations of the PSF pattern. It was originally proposed by Sparks and Ford [2002], and later refined by Thatte et al. [2007], to extend its usage to detect close-in companions using iterations to minimize self-subtraction effects on possible companions. However, we feel that the term Spectral Differential Imaging (SDI) is more appropriate than ``spectral deconvolution'' because

the chromatic variations of the stellar PSF can be post-processed into a radial displacement of the astrophysical source with a constant PSF.

Here we apply PCA to obtain the PSF model using the radial sampling in SDI. We also consider channel selection of reference PSF samples with wavelength ratios matched to the radial diffraction shifts. This radial sampling provides an improvement in throughput by a factor of roughly 2 in the case of our application. We refer to this improvement as local Spectral Differential Imaging (l-SDI).

The first two Chapters present the background for high-contrast imaging: Chapter. 2 gives a summary of the observations techniques that historically have been used for high-contrast imaging. Chapter. 3 summarizes the main methods for speckle and PSF subtraction. In Chapter. 4 we give a brief description of the dataset obtained by the integral field spectrograph (IFS) at the VLT/SINFONI [Bonnet et al., 2004; Eisenhauer et al., 2003] and the simulation of fake companions to characterise the technique. In Chapter. 5 we present an overview of the SDI technique and our new approach. In Chapter. 6 we show our results in terms of detectability and flux throughput and we apply the technique in SINFONI data. Finally Chapter. 7 contains general discussions.

Chapter 2

The optical problem and observational techniques

The follow chapter was extracted from [Oppenheimer and Hinkley, 2009] review.

2.1 The optical problem

The main issue when observing the circumstellar surroundings of a star is the residual starlight that contaminates the Field of View (FoV). This contamination comes from two principal sources: light due to optical diffraction, and due to imperfect optics combined with the propagation of light through a turbulent medium.

2.1.1 Diffracted Light

For a perfect image, i.e. limited only by diffraction due to the optical system, the point spread function (PSF) is known very accurately. For a circular aperture it correspond to an Airy pattern. So one could simply subtract the known PSF from the image, and the residuals will show whatever is lying underneath. But perfect observations are not achievable in reality. They would require long integration times to measure the light of the star and to get sufficient signal on the PSF to detect small `perturbations`. One can remove this diffracted light with two classes of techniques, coronography and interferometry, that will be briefly addressed in Secs. 2.2.2 and 2.2.3 respectively .

2.1.2 Speckles

The incoming wave front of light is never perfectly flat because no imaging system is perfect. It will always have small wave front errors. Typically the quality of an image is measured by the ``Strehl ratio", S, that is defined as the ratio of the peak intensity in a real image to that of a perfect image made with the same imaging system's fundamental parameters. The Strehl ratio is often approximated to

$$S \propto \ exp(-\sigma^2), \tag{2.1}$$

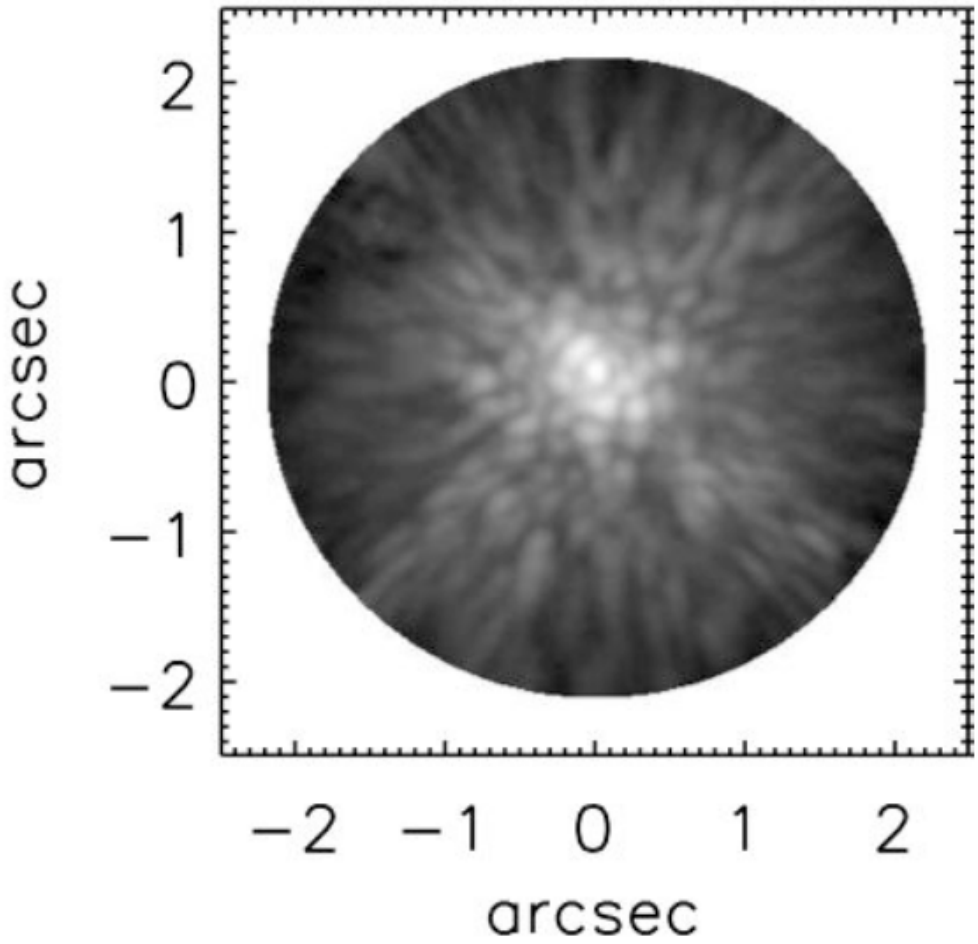

Figure 2.1: Image in H-band using a coronograph from Hinkley et al. [2007]. Showing the high prevalence of the speckle pattern, even in a high quality image (S=85%).

where σ is the root mean square of the wave front error in radians (when $\sigma \ll 1$).

For example, a good typical value of S is 70%, that means that 30% of the starlight will be distributed over the FoV in a non-uniform and complex pattern called speckles (see Fig. 2.1).

To understand how this speckle pattern is formed, Stapelfeldt [2006] uses a simple approach with a Fourier approximation. It predicts that this speckles will appear at almost arbitrary locations in the image each with different intensities (as seen in Fig. 2.1). Their positions are a function of the wave front perturbations and the wavelength.

Speckles don't follow the Poisson statistics, and their noise contribution is several orders of magnitude larger than the Poisson noise of the ideal PSF [Racine et al., 1999]. Their noise is highly correlated [Soummer et al., 2007]. So increasing the exposure time to get a higher signal to noise (S/N) will not work, because the speckle noise can't be averaged out once the speckle lifetime is reached [Hinkley et al., 2007]. These lifetimes can vary from few milliseconds to ten seconds, and some of them can even last many minutes at $0.5\mu m < \lambda < 2.5\mu m$ [Hinkley et al., 2007].

2.2 Observational techniques

2.2.1 Adaptive Optics

The term adaptive optics usually refers to a set of procedures and techniques that aim at getting diffraction-limited images from a telescope. We won't discuss this subject at length, but we will give a notion of it in the context of high-contrast imaging.

A standard AO system has two main stages. First a tip/tilt system corrects for large movements of the PSF due to atmospheric turbulence or vibration of the telescope. Second, with the image stabilized by the tip/tilt system, the lower-order corrections are made with a deformable mirror. These mirrors can have up to thousands actuators underneath them [Dekany et al., 2006]. For this actuators to work, and deform the mirror to correct by the wave front, a `guide star` is needed to retrieve the wave front shape from a sensor at rates of thousands times per second. The faster the sensor the better the correction is performed, but a brighter guide star is needed.

AO allows us to achieve diffraction-limited images, but we still need to get rid of the diffracted light. Two additional observational techniques aim at suppressing this light: coronography and interferometry.

2.2.2 Coronographs

The classical Lyot coronograph uses two masks to suppress the starlight Fig. 2.2. The first mask takes place where the image is formed, the focal plane, and is a small circular star-centred mask of diameter about 3-6λ/D, which absorbs most of the starlight and the rest diffracts around it. The image is then put out of focus and an image of the telescope pupil forms. In this image two rings are formed containing most of the diffracted light. Here lies the advantage of this design. The light that is not diffracted by the first focal mask, will be uniformly distributed. But the light from the star will diffract into an outer and inner ring that can be masked again ,with the Lyot mask, to eliminate the light from the star. Finally the image is brought back to focus with $\sim 99\%$ of the star flux reduced, leaving any object close to the star minimally reduced. Nowadays we found many different improvements of this classical model in the literature. But for the propose of this thesis, they are irrelevant. Guyon et al. [2006] provides a wide treatment of 16 different coronographic techniques and compares them.

2.2.3 Interferometry

The application of optical and infrared (IR) interferometry to the high-contrast problem is relatively new compared to coronographs and AO. It is a powerful technique for searching emission sources very close to the star, since it can achieve far higher angular resolution than ground based direct imaging. We won't discuss interferometry further in this thesis. We refer the reader to Beuzit et al. [2007] who provides a good review of interferometry applied to high-contrast observations, and two examples of detections in these kind of observations may be relevant to this work [Biller et al., 2012; Huélamo et al., 2011, companion candidates in HD 142527 and T Cha].

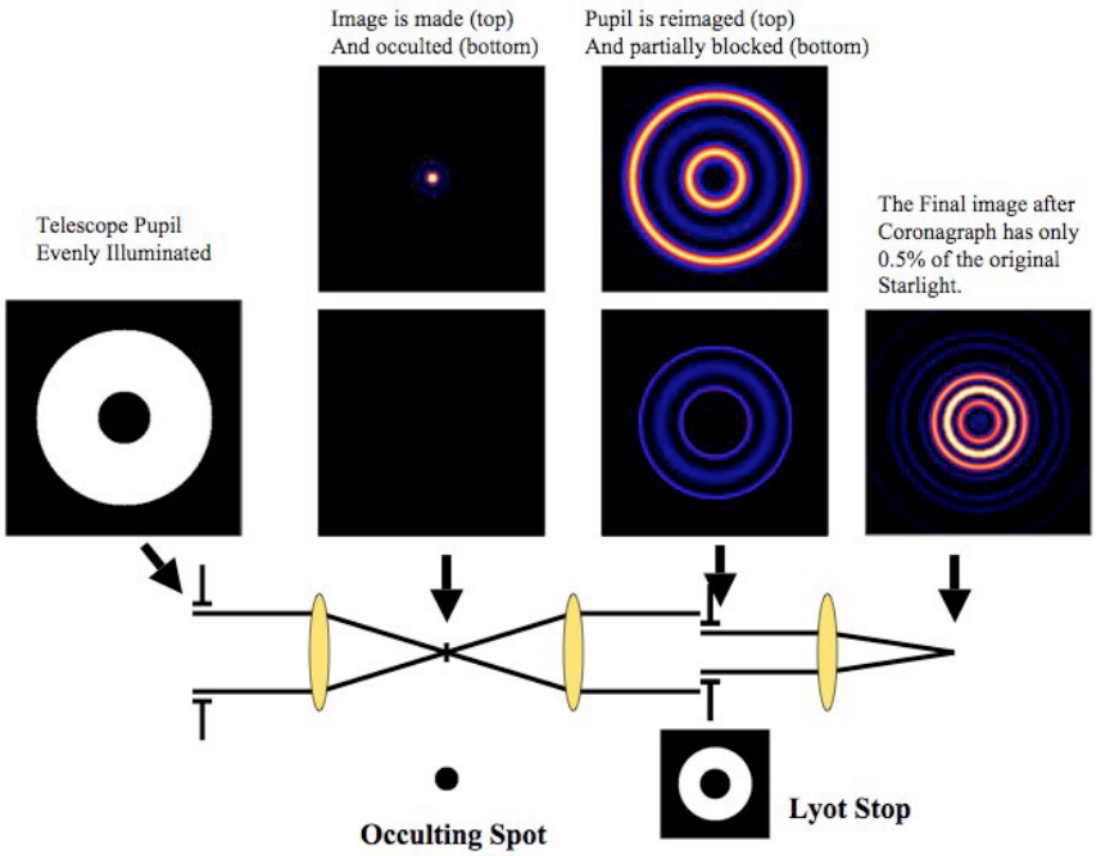

Figure 2.2: Simplified diagram of a Lyot coronograph, assuming a flat wave front. [Oppenheimer and Hinkley, 2009]

Chapter 3

Image processing methods

In the previous chapter, we discussed the main observational methods for high-contrast imaging. We stated that image processing after obtaining the data with AO is essential to reach the high-contrast levels required to faint companion detections. In this chapter we discuss the main imaging methods that can remove the remaining speckle pattern and the diffracted-limited PSF by subtracting a reference image. This chapter was extracted mainly from two reviews Oppenheimer and Hinkley [2009]; Wright and Gaudi [2013].

3.1 Polarimetric differential imaging

The main principle behind this method, is that starlight is not polarized, so polarimetric observations will not be affected by the residual pattern of speckles. Using double-differential polarimetric imaging and taking simultaneous observations of different polarization states [see Kuhn et al., 2001], one could image circumstellar disks and possible companions because dust grains and exoplanets will scatter starlight, inducing polarization. Examples of imaging with this technique can be seen in [Canovas et al., 2013; Follette et al., 2013; Oppenheimer et al., 2008; Perrin et al., 2004]. A recent polarimeter, designed to be used in polarimetric differential imaging (PDI), is presented in Rodenhuis et al. [2012].

3.2 Reference star differential Imaging

Reference star differential Imaging (RDI) is the least elaborated of the methods. It basically consist in subtracting a reference PSF from a reference star [Marois et al., 2005] to the target image. The efficiency of this method depends on how much correlation exist between the reference and the image. And this depend on time delay between the acquisition of both, the reference star and the target, because the stability of the speckles varies within a timescale, i.e the lifetime of the speckles (see Sec. 2.1.2). One of the main problems of this approach is to find a reference star compatible with our target. This star has to have similar stellar properties (magnitude, color). Otherwise AO corrections won't produce a similar residual speckle patterns. Besides the reference star has to be close enough to the target, to be able to take exposures of both of them in a timescale, at least of the same order or less than the average lifetime of the speckles. Nevertheless this method is advisable when the others cannot be applied [Mawet

et al., 2012, e.g. coronography data at close angular separations].

3.3 Angular differential imaging

Angular differential imaging (ADI) [Marois et al., 2006] is a powerful method to estimate a reference PSF from the target without the need of a reference star. This method takes advantage of the rotation of the FoV with respect to the telescope pupil when a sequence of observations are taken with the instrument rotator turned off or adjusted to keep the instrument and telescope optics aligned. This will cause a low rotation of the FoV through the sequence of observations. For each image a reference PSF is subtracted from the other images of the same sequence. If the FoV rotates enough, the signal form the companion will be preserved after the subtraction. After each image have been subtracted, they are all rotated to align the FoV and a median is extracted. Several improvements on this basic scheme have been made, among them Lafrenière et al. [2007] uses a 'locally optimized combination of images' (LOCI), a linear combination of selected images within the observation. The state of the art is to estimate the PSF using principal component analysis (PCA) (see appendix8), an application of this can be found in two algorithms PynPoint and KLIP[Amara and Quanz, 2012; Soummer et al., 2012, see]. We will further describe ADI later on.

3.4 Simultaneous differential imaging

It was first suggested by Racine et al. [1999], to subtract two simultaneous observations in different but close wavelengths across the methane band ($1.59\mu m$), thus revealing any companion containing methane. The wavelengths must be close enough for the two PSF's to be highly correlated, and the images must be simultaneous to prevent the pattern of speckles from changing. Examples of implementing the simultaneous differential imaging (SDI) are the TRIDENT instrument [Marois et al., 2005] and the simultaneous differential extrasolar planet imager at the VLT [Biller et al., 2006].

3.4.1 Spectral deconvolution or spectral differential Imaging

As ADI takes advantage of the azimuthal differentiation that rotates the FoV, the introduction of an integral field spectrograph (IFS), allow us to take advantage of the chromatic properties of speckles and the PSF in such a way that we will have radial movements of the diffraction pattern as a function of wavelength. The IFS provide a 3D data cube, which contains the spectral information of a plane in the sky. Both the Speckles and the PSF scale linearly with wavelength ($\sim \lambda$), so if we scale the image we can align the PSF features and the speckles, while the FoV will be radially differentiated (same as ADI but not azimuthally). We can later estimate the PSF in each spectral image and subtract it by various methods we will discuss later on. Finally the spectral images are scaled back . One of the most convenient aspects of this treatment is that if a companion is detected its spectral information is a by-product. This was first proposed by Sparks and Ford [2002] as the spectral deconvolution (SD) technique. Although other authors referred to it as SDI-IFS, we feel it should be just SDI, but after spectral differential Imaging.

3.4.1.1 d-LOCI

As ADI, since SD or SDI was first proposed by Sparks and Ford [2002], its basic scheme remains the same, but there have been many ways to determine the way to select an optimal reference PSF. Recently Pueyo et al. [2012a] have developed a variation of LOCI, damped LOCI or d-LOCI. It was applied to data from an IFS under the same principle of Sparks and Ford [2002], but with a constrain in its optimization coefficients.

Chapter 4

Data reduction and fake companions

We selected a sample of young stellar objects (YSOs) with circumstellar disks with documented evidence for gas and disk gaps, and a single central star. Data were acquired using the SINFONI integral field spectrograph at the 8.2 m telescope UT4 (Yepun) of the VLT at Cerro Paranal Observatory. SINFONI can be fed by an adaptive optics (AO) module and operates in the J, H and K near-infrared bands (1.1-2.45 μm), with spatial resolutions of 250 mas, 100 mas and 25 mas.

Source	Grating	Scale	DIT	Expousures	Dates	OB number
CS-Cha	K	0.025	20s	5	9 Mar. 2012	200226132
CS-Cha	H+K	0.025	20s	5	9 Mar. 2012	200226132
SZ-Cha	H+K	0.025	4s	10	9 Mar. 2012	200226137
T-Cha	H+K	0.025	4s	5	9 Mar. 2012	200226138
HD 100546	H+K	0.025	4s	5	9 Mar. 2012	200226140
HD 142527	H+K	0.025	100s	16	9 Mar. 2012	200226145
HD 142527	H+K	0.025	100s	7	9 Mar. 2012	200226147
HD 45677	H+K	0.025	1s	2	9 Mar. 2012	200226170
LkCa15	H+K	0.025	15s	2	10 Mar. 2012	200226173
T35	H+K	0.1	50s	5	10 Mar. 2012	200226179
HD 142527	H+K	0.025	300	7	12 May 2012	769575
HD 142527	H+K	0.025	300	7	11 Mar. 2013	769574
HD 142527	K	0.025	100	5	7 May 2013	769573
HD 142527	K	0.1	300	4	7 May 2013	769573
HD 142527	K	0.025	100	5	18 Jun. 2013	769572
HD 142527	K	0.1	300	4	18 Jun. 2013	769572

Table 4.1: Summary of observation with SINFONI. At this stage we have only applied l-SDI succesfully to HD 100546, T-Cha, and the observations of HD 142527 from 9th of March 2012.

The observations selected for this work were spread over 2012 and 2013 (see Table 4.1). We chose to work on HD 100546, T Cha and HD 142527.

HD 142527 was observed on May 2012, March 2013, May 2013 and June 2013 with two spatial resolutions of 100 mas and 25 mas (corresponding to field of views of $3" \times 3"$ and $0.8" \times 0.8"$, respectively) using the H+K grating, leading to a spectral resolution of R$\sim$1500. Two other runs of 25 mas of spatial resolution were taken in May 2013 and June 2013, but using

the K grating, corresponding to a spectral resolution of R$\sim$3000. They were taken with a shift in P.A. of $\sim 45°$, thus changing the orientation of the PSF features.

The 25 mas spaxels oversample and better describe the PSF. However, the 100 mas spaxel provide a larger field of view (FoV), which is also required in SDI to sample the PSF for a wide spectral coverage. The H+K grating is better suited for SDI because the technique is more effective with a wide spectral range [Thatte et al., 2007]. The run for HD 142527 was carried out by mosaicking in a 2$\times$2 pattern with two different strategies: we covered each corner in separate observing blocks, and also looped over each corner in the same observing block. We typically used detector integration times (DIT)s of 4s, with 50 coadds (i.e. NDIT = 50), for tiles where the star fell on the array, and DITs of 300s, NDIT = 1, when the star was off the array.

ESO observatory provides a pipeline for the reduction of SINFONI data. We drove the observatory pipelne version 2.3.3 with `esorex` and a set of home-made scripts in the Perl. Exposures of standard stars with matched elevations where acquired for the correction of telluric features.

In order to implement the simulations presented here we used the HD 142527 (see 4.1, OB number 200226147) data set, because it has a larger FoV and does not seem to have any bright signal in its residual image after our early tests. Fake companions were created in each channel of the HD142527 spectral cube at differents angular separations. We fited an airy pattern to the central star and used these parameters to make the artificial companion, see Figure 4.1.

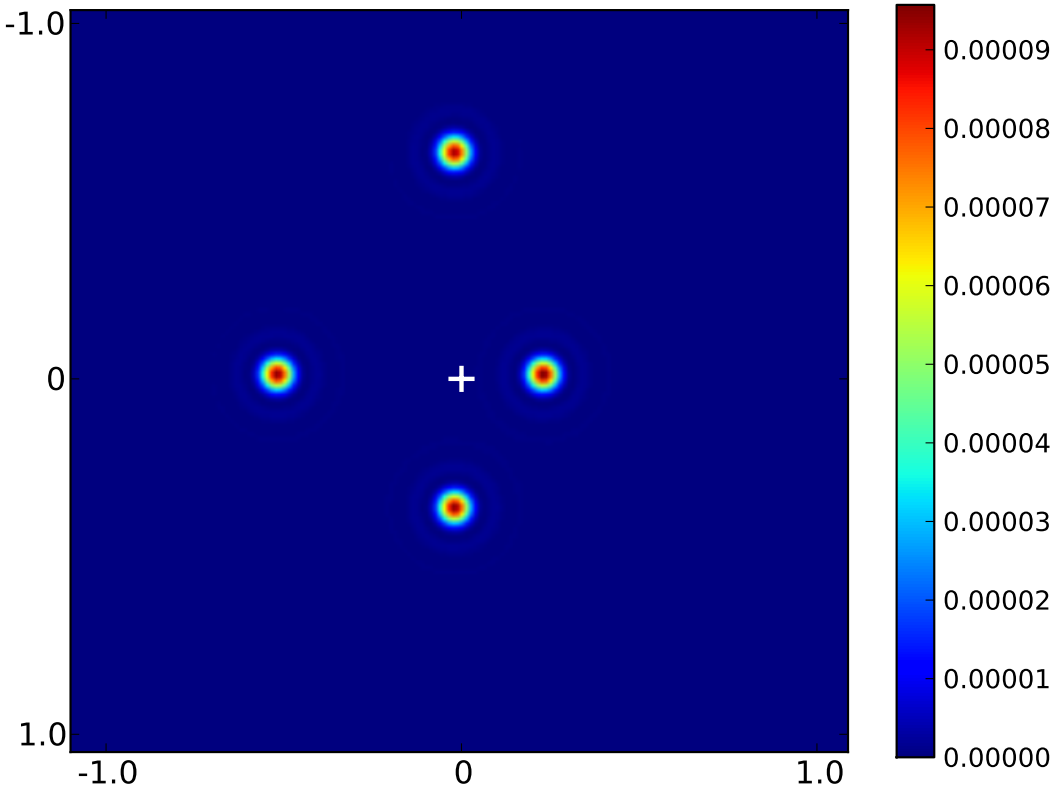

Figure 4.1: Fake companions at 0.251'',0.375'',0.500'' and 0.625''. We chose this angular pattern to to avoid overlaps while working with several fake companions simultaneously.

Chapter 5

Overall view of the technique

It is possible to characterise the PSF, i.e. the image of the stellar point source on the detector array, as an Airy pattern with characteristic rings separated by $W \propto \lambda/D$, together with a pattern of secondary images, or speckles. These speckles are produced due to scattering of the irregular wave-front [even in an ideal AO system Macintosh et al., 2006], also of typical dimension λ/D. So we expect that the PSF will approximately scale with wavelength, such that the speckle pattern will swell linearly with wavelength. This scaling law is only approximate because the Strehl ratio decreases with wavelength. Here we exploit this wavelength dependence of the PSF, i.e. the PSF chromaticity [e.g. Pueyo et al., 2012b], to infer a PSF model for the subtraction of the stellar PSF.

Since the airy rings and speckle pattern scale linearly with λ, at least to first order, it is necessary to shrink each image at a given wavelength plane so that the speckle pattern is kept approximately constant along the wavelength axis. For example, if we take the first image is at $1.4\mu m$ as reference wavelength, the image at $2.0\mu m$ should be shrunk by a factor of $1.4/2.0$.

With a scaled data cube we can estimate the PSF by three different ways:

1. *Median Estimate:* The first approach is to obtain a model of the PSF by taking the median of the scaled cube along the wavelength axis. To perform the subtraction of the stellar PSF this median-estimated model is then subtracted to each wavelength channel after scaling in intensity by linear regression. After performing initial tests using this median PSF model, we found that it provides a much lower throughput than the alternatives. Accordingly we did not further develop this technique.

2. *Polynomial fitting in wavelength:* According to Sparks and Ford [2002], the classical SDI technique fits a low order polynomial in each pixel of the scaled cube along the wavelength, and constructs a PSF for each channel with this model. The assumption is that a low order polynomial will not pick up the small modulations injected by the companion candidates [Sparks and Ford, 2002].

3. *Principal Component Analysis:* We can also view the wavelength dependence of the PSF as a set of sample PSF measurements with which to build an orthogonal basis set. The Principal Component Analysis is well suited to generate such a basis set. The projection of the data cube onto the PCA basis provides ordered components; the first few components already provide a model of the PSF. We select the first K components to construct a model

PSF in the form

$$\mathbf{I}(\lambda) = \sum_{i=1}^{K} a_i(\lambda) C_i,$$

where C_i are the principal components that form the orthogonal basis. This PCA decomposition provides a model data cube that approximates the bulk of the data for each wavelength plane. Since the stellar PSF represents the bulk of the signal, it is hoped that a number of components K can be found that does not incorporate signal from the companions. Including more components gradually improves the model of the data, and eventually picks up the companion signal (which in this scaled data cube is spread radially). As explained in Sec. 1 PCA has recently been used by Amara and Quanz [2012]; Soummer et al. [2012] to create an orthogonal basis sets for the ADI technique.

After subtracting the stellar PSF, through either technique, the subtracted data cube is then rescaled spatially to the original pixel scale. This PSF-subtracted data cube can then be collapsed for the detection of faint signal, or else to extract spectra from known faint companions.

5.1 The code and PCA

The code was written in python using the AGPY package by Adam Ginsburg and scipy libraries. Following the algorithm proposed by Sparks and Ford [2002] the cube must be scaled to align the PSF. Firstly, we must be absolute sure that the image is centred. To centre the cube, there were two possible methods: fitting a simple Gaussian in each channel, finding the centroid and then aligning all the images; or maximizing the cross-correlation function between each channel. To find the maximum it is enough to fit a Gaussian to the cross-correlation matrix. We choose to fit a Gaussian in each channel, and then use a local regression to construct the wavelength dependence in the center of the PSF in each channel.

Sometimes the center of the star will not be available in the FoV of the observation (see Appendix 8).

With every channel in the cube adequately aligned we can proceed to spatially scale each wavelength plane. The code uses the `ndimage` package in `scipy` to shrink and shift the image using an `spline` interpolation scheme.We chose the lowest wavelength of the data cube as the reference wavelength $\lambda_\circ$. To shrink the image from the plane at wavelength λ_i we used a geometric transform that shrinks the cube by a factor of $\lambda_\circ/\lambda_i$.

According to Thatte et al. [2007], the radial limit to which a companion candidate can be detected is a function of the maximum and minimum wavelength of the cube, because it is constrained by a lower limit in the radial displacement of the companion when we spatially scale each wavelength plane by $\lambda_\circ/\lambda_i$. Let $\Delta\theta_c$ represent this radial displacement at the separation θ_c. If we assume that the width of the companion is given by the first null of the airy diffraction pattern, i.e. $2 \times 1.22\frac{\lambda}{D}$, the radial displacement $\Delta\theta_c$ must be large enough so that some wavelength planes of the the scaled cube are entirely devoid of companion light [see Thatte et al., 2007, their Fig. 1].

Following Thatte et al. [2007], the radial displacement $\Delta\theta_c$ can be parametrised as

$$\Delta\theta_c = 2\epsilon \times 2.44\lambda_\circ/D$$

where the parameter $\epsilon > 1$ means that at least some of the channels are free of companion

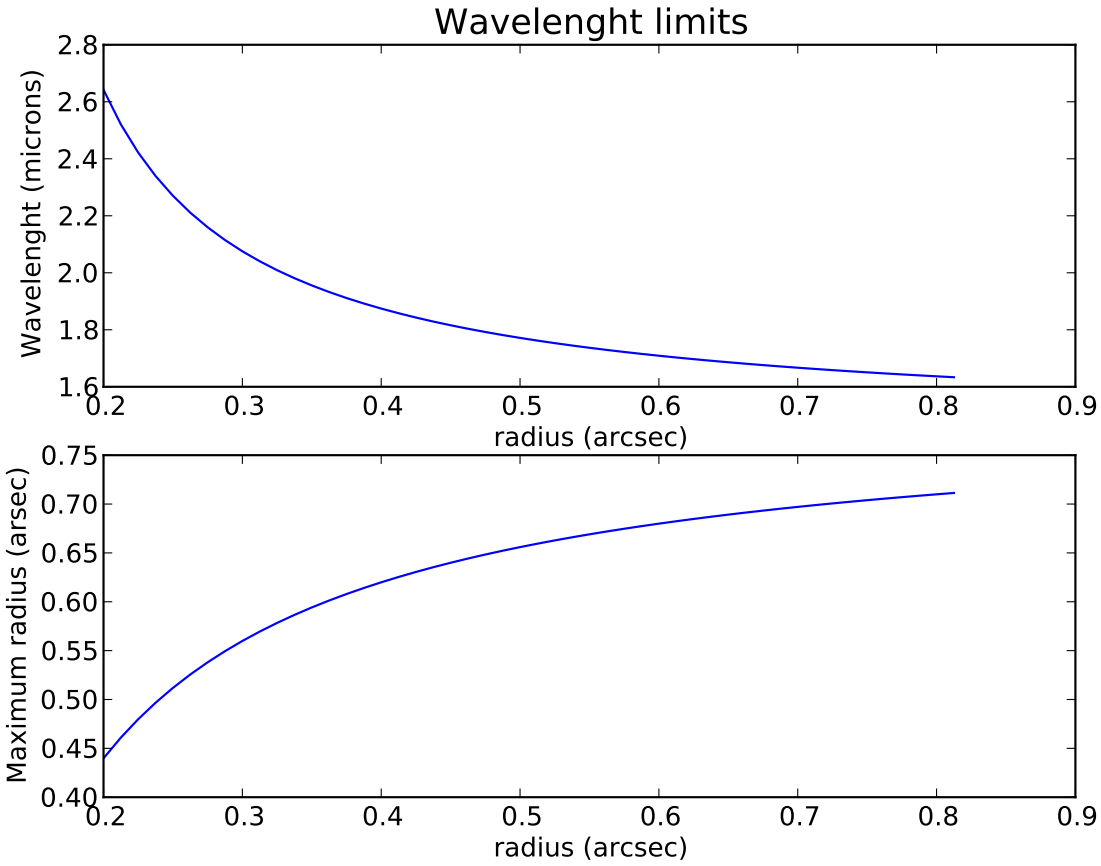

Figure 5.1: Constraints using $\epsilon = 1$ as a threshold. The upper graphic shows the minimum upper wavelength (with $\lambda_\circ = 1.4525$ as the lower one) that meets the $\epsilon = 1$ criterion at that radius, i.e. the radial movement of the companion along the cube is the minimum displacement for a PSF stack not entirely contaminated by the companion flux in each pixel. And the lower graphic shows the maximum radius at which a point source will not fully contaminate the whole spectrum as a function of the spectral width (this wavelength is determined by the upper graphic, i.e. the minimum inner radius), see Thatte et al. [2007, fig.1] for a scheme of the cube contamination.

light at the separation θ_c. Fig. 5.1 shows the minimum wavelength range the data cube has to have to detect a point source close to the star if the data cube starts at the beginning of H band ($\lambda_\circ = 1.4525\mu m$). Fig. 5.1 also shows the maximum radius from which we can estimate the PSF in all of the spectral channels, which is limited by the spatial scaling, for a given range in wavelength. The inner and outer regions where the PSF can be successfully modelled, will depend on both the spectral range and the spatial size of the cube.

5.1.1 Polynomial Fit

One possible way to estimate the PSF is to fit a robust low-order polynomial to the spectrum extracted in each spatial pixel. This approach was first proposed by Sparks and Ford [2002]. Since the radial displacement of a faint companion represents a high frequency component in the signal compared to the smooth PSF variations with wavelengths (that mostly stem from varying Strehl ratio), the low polynomial will not pick up the companion light.

The polynomial fit is weighted by the spectrum of the STD star. Since we are working with two bands (H+K), this weighting scheme naturally avoids the region between both spectral windows.

We thus obtain a new cube containing a model of the PSF in each channel. To improve the final contrast a linear regression is performed to further fit the PSF model to each channel. The code uses the Kendall-Theill robust linear fitting algorithm to perform the regression between the model and the data.

5.1.2 Principal Component Analysis

Another way to estimate the PSF is to build an orthonormal basis set using Principal Component Analysis (i.e. the discrete Karhuenen-Loève Transform). It has been applied before by Amara and Quanz [2012](PynPoint) and Soummer et al. [2012](KLIP) to ADI observations. For a full description of PCA and how it is applied (see appendix 8).

5.2 Selecting the number of principal components to our model

To estimate de number of PCA components to use in the RDI technique, we use the Akaike Information Criterion (AIC). The number of PCs is treated as a parameter in [Amara and Quanz, 2012] and Soummer et al. [2012].

This criterion was first proposed by Akaike[Akaike, 1974] ,and a variation of the criterion by Schwartz and Rissanen, MDL (Schwarz [1978], Rissanen [1978]).It can be applied to select the optimal number of independent signals, to model an observation vector. Wax and Kailath used this criterion to determine the number of independent signals in their model, with no subjective judgement in the decision process [Wax and Kailath, 1985]. This number is determined by the minimization of the AIC or MDL criterion. The determination of the number of independent signals, in this problem, reduces to determine the number of principal components to be used in the PSF model. We proceed as Wax and Kailath did but with our vectorised images (see appendix .2). When applied to the entire cube of data AIC gives a minimum at $k = 35$, i.e. we need only the first 35 principal components.

5.3 Local spectral differential imaging (l-SDI)

Current SDI (or spectral deconvolution) techniques for the subtraction of the stellar PSF, use a PSF model that is not contaminated by the companion flux. In order to get a clean detection, ideally a reference PSF is used for ADI reduction (Thatte et al. [2007], Lafrenière et al. [2007]). LOCI constructs a reference PSF free from a possible companion contamination, and PynPoint states that there is a chance that the possible companion will be self-subtracted, if the PCs accounts for some of its flux.

For ADI observations, the *angular movement* across the PSF is quite a lot, depending on the time interval τ, thus providing a set of PSFs that are easily not entire contaminated by a possible point source. On the other hand, the *radial movement* in the SDI technique is much less than the movement in ADI, thus constraining the width of the bands used (see section 5.3.3).

5.3.1 Non-linearity of the PCA-filtered response to a point source

The response of the SDI technique, in terms of throughput, is not the same for companions with different input flux, or angular separation from the central star. In order to characterise this response, and as a measure of the effectiveness of this technique, we ran simulations by injecting fake companions in the science data.

The HD 142527 data were selected for these simulations because it has the biggest FoV. A total of five fake companions were injected at 0.12", 0.25", 0.42", 0.5" and 0.62", using an airy pattern with its parameters taken from a fit to the star in each channel (width_x, width_y, height, amplitude, rotation). We used 1%, 0.5%, 0.1%, and 0.01% (corresponding to 5, 5.7, 7.5 and 10 magnitudes) of flux contrast. We estimate the throughput as the ratio between the peak of the collapsed emission in the residuals, and the peak of the collapsed emission in the input fake companion. The collapsed emission is calculated as the median of the spectral planes of the cube data, i.e. the collapsed cube. In Fig. 5.2 we show plots of the throughput for both SDI techniques, using PCA and the polynomial fit. We find an increase of the throughput by a factor of $3-5$ in the outer regions of the disk, when applying the SDI algorithm instead of the polynomial fit.

All these reductions were made with just two principal components. It may be possible to improve the residual noise by increasing the number of principal components used as the fake companion gets fainter. The PCA analysis is susceptible to copy, in the first few principal components, the flux of strong companions if they are present as shown in Fig. 5.3. But as they get faint one could use more components with minimal flux loss, this problem is address in Sec. 5.4.

From Fig. 5.4, the point source in the residual images looks shattered and its flux is spread radially. This complicated transfer function injects structures that differ from the input point-source profiles. Therefore it may not be adequate to estimate the throughput as the ratio between the peaks (see Chapter. 7).

Statistically, in Figs. 5.4(e) there is no 3-σ detection if we compare the peak of the signal to the rms in a one-stellar-FWHM-wide, Δ_*. Yet visual inspection reveals a response from the point source.

If the response can be characterised, then the fainter response can be compared to a sure detection (for example a 1% contrast detection). But from the values of the slope errors from 5.3.1 and 5.3.1 we can see that the response is not linear at all. This is to be expected due to

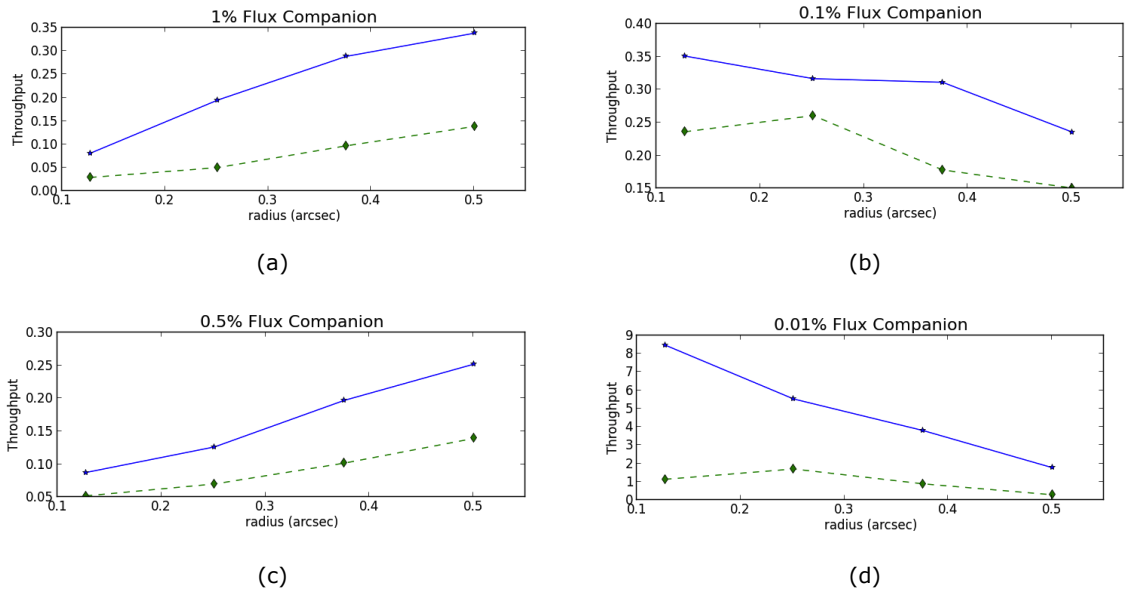

Figure 5.2: Throughput of different companions and contrasts, in HD 142527 data cube. This throughput was calculated as the ratio of the signal peaks from a collapsed cube, i.e., the mean of all spectral planes.Figs. 5.2(a), 5.2(b) show companions having 1% of the host star flux, showing a clear tendency of increasing throughput towards the outer parts of the disk. Nevertheless, Fig. 5.2(c) does not show this tendency, probably because the signal to noise is too low. Same happens with Fig. 5.2(d), that is completely dominated by the noise.

the nature of the PCA analysis, which can absorb point source signals in the PSF model if they are contaminating our reference stack of PSFs [see also Amara and Quanz, 2012, for the ADI case].

In order to circumvent the above difficulties in SDI, in what follows we investigate the selection of reference channels that allow to build a PSF model devoid of companion light.

5.3.2 Channel selection of reference PSF samples

We apply a selection process to determine which PSF reference images can be used without introducing self-subtraction. It is similar to the one used by Pueyo et al. [2012a].

Consider an annular section at a fixed radius r, with a width δr, as shown in the Fig. 5.5(a). Consider also a possible companion at $r = 37\ mas$. From Fig. 5.5(a) we can see that the annular region containing the PSF at a radius r in the spectral plane λ_m, will shrink and expand through the cube, due to the wavelength dependence of the Airy pattern and the speckles. In others words, at $\lambda_{\text{inner}} < \lambda_m$, the δr region in λ_m, will be shrunk by a factor of $\lambda_{\text{inner}}/\lambda_m$. And at $\lambda_{\text{outer}} > \lambda_m$, the δr region will be expanded by a factor of $\lambda_{\text{inner}}/\lambda_m$.

After scaling the cube, the δr region will align in all the spectral planes. But the companion will be shifted towards the central star in λ_{inner}, and outwards in λ_{outer}. We can choose a certain $\lambda_{\text{inner}*}$ and $\lambda_{\text{outer}*}$, that leaves the annular region where we seek to estimate the PSF *free* from a possible companion. We can then select the channels with $\lambda < \lambda_{\text{inner}*}$ and the channels with $\lambda < \lambda_{\text{outer}*}$, to form two sets of reference PSFs to the annular region at λ_m (the *inner* and *outer* set respectively), that are *free* of a possible companion's flux. We called this algorithm local spectral differential imaging (l-SDI).

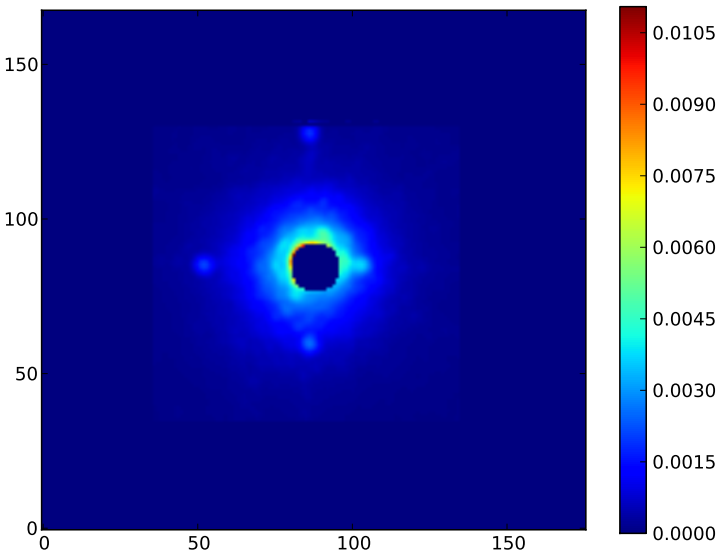

(a)

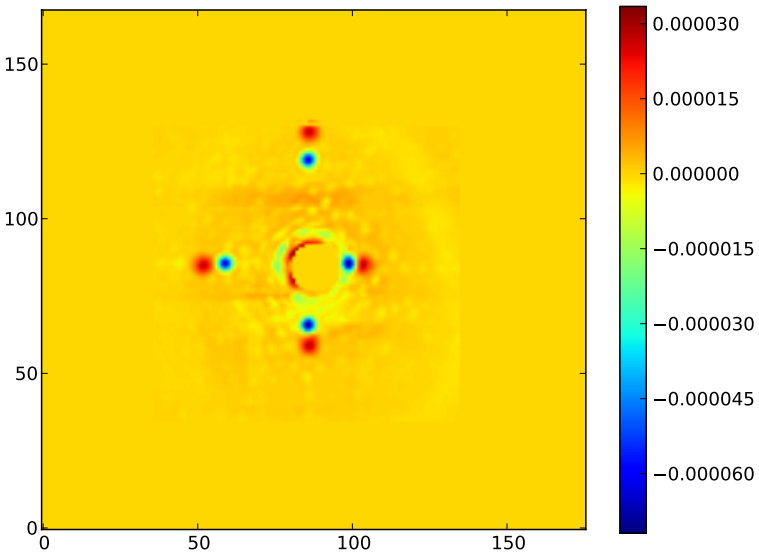

(b)

Figure 5.3: First two principal components of companions with 1% of the flux . Fig. 5.3(a) is the first principal component. Note that in the second principal component, Fig. 5.3(b) the companions are clearly copied, due to the high flux of these companions.

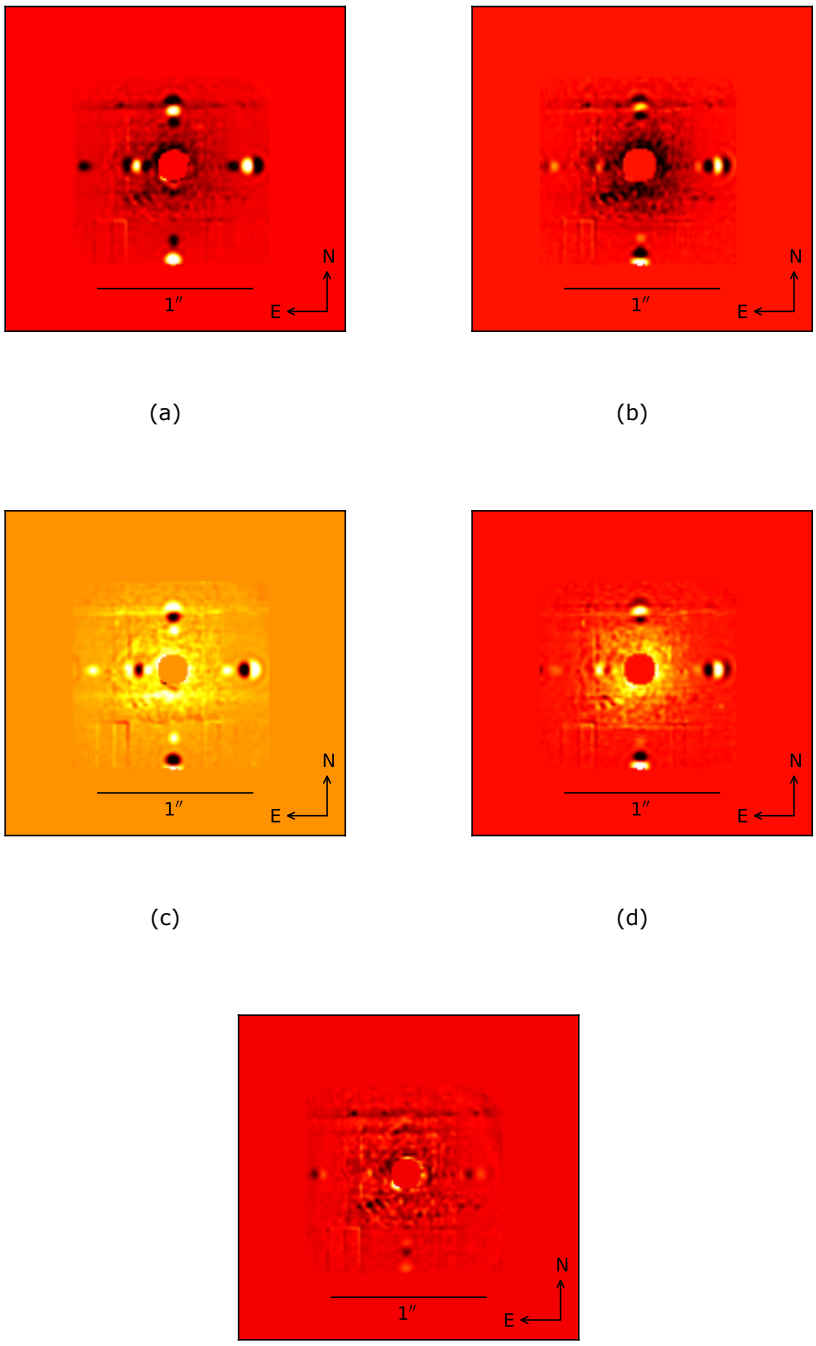

Figure 5.4: The 5.4(a) panel contains the residuals of PCA, and the 5.4(a) panel contains the residual of polynomial fit, with companions of 1% of the stellar flux, both in one channel of the H band. The 5.4(c) and 5.4(d) show same reduction (SDI and polynomial fit, respectively) but in just one channel of the K band. The 5.4(e) panel shows a fainter companion after PCA, with 0.05% of the star flux.

Planet	Angular separation (arcsecs)	χ^2	α_{slope}
1	0.251	1.17	0.426±0.088
2	0.375	1.13	0.106±0.158
3	0.500	0.66	0.071±0.147
4	0.625	0.17	0.054±0.019

Table 5.1: Linear regression of output signals of 0.1% of the flux to a *clear* detection of 1% of the flux.

Planet	Angular separation (arcsecs)	χ^2	α_{slope}
1	0.251	0.38	0.030±2.982
2	0.375	1.47	0.001±3.550
3	0.500	0.01	0.006±0.470
4	0.625	0.16	0.008±0.167

Table 5.2: Linear regression of output signals of 0.01% of the flux to a *clear* detection of 1% of the flux. Errors to calculate the χ^2 reduced where widely overestimated since we use the rms of an annular region that contains a high degree of artificial features. We can see from the errors of α_{slope} (they are much higher than the actual value of α_{slope}) that the response of the SDI technique is not linear.

To apply the AIC criterion we need enough PSF references in both sets. Empirically 75 reference PSFs from the channels with $\lambda < \lambda_{\text{inner}*}$ and 75 from the channels with $\lambda > \lambda_{\text{outer}*}$ will be sufficient.

We need to avoid unnecessary operations in each computational loop. Since we need to find a set of reference PSFs for each δr in each channel, the computational time that this algorithm takes is much longer than SDI. We parallelize the code of l-SDI between sixteen cores using the multiprocessing module in python, which dramatically decreased computational time.

5.3.3 Inner working angle

There is an intrinsic limitation to detect close-in companions with l-SDI. Given a radius r in a channel with λ_* there is a maximum radial shift of the PSF features that is determined by the first (λ_1) and last (λ_2) channels available in the spectral sample. Namely, the PSF features can expand by a factor of at most (λ_2/λ_*) and contract by a factor of at most (λ_1/λ_*). In the SINFONI data these channels correspond to $\lambda_1 = 1.437\mu m$ and $\lambda_2 = 2.460\mu m$. In what follows we determine the minimum angular separation at a channel λ_* that can be modelled by l-SDI by requiring at least one spectral channel to build a reference PSF that is *free* of a possible companion's flux.

Let λ_m be any spectral plane in the cube, and λ_i and λ_f be the inner and outter planes that we will use to construct the reference PSF, respectively. The *inner* spectral plane ($\lambda_i < \lambda_m$) will expand by a factor of λ_m/λ_i to match the PSF at λ_m, and the outer spectral plane (λ_o) will shrink by a factor of λ_m/λ_o to match the PSF at λ_m (see Fig. 5.5). As the cube shrinks and expands the companion will 'move', inwards at the outer spectral plane (λ_o) and outwards at the first one (λ_i). We required this displacement to be enough to obtain a reference PSF that is partially, if not completely, *free* of a possible companion's flux in the annular region of interest. We choose a partial limit displacement of one HWHM, because in this way every pixel

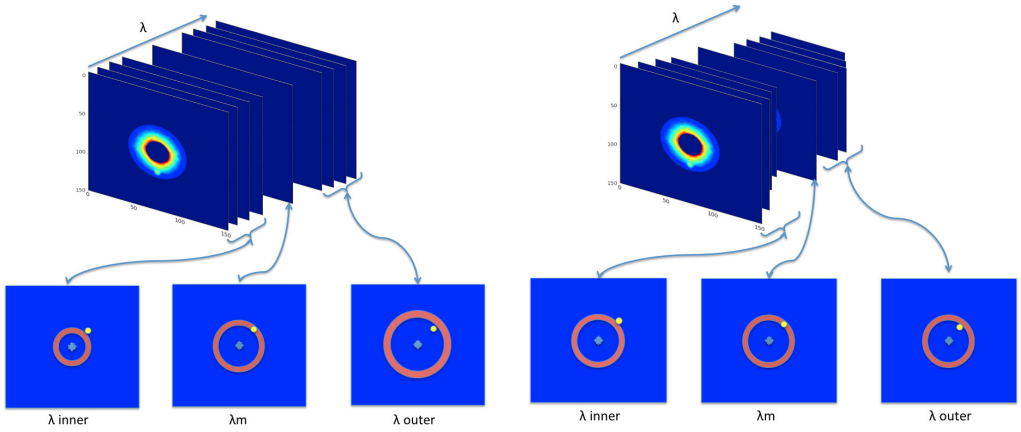

(a) (b)

Figure 5.5: Schematic Diagram of the annular regions to be used. The left panel 5.5(a) represents the cube before the scale was applied, and the right panel 5.5(b) represents the cube afterwards. The main goal is to select a subset of the spectral channels to serve as PSF references in a narrow annulus, that due to the scaling would not have flux of a potential companion, thus reducing self-subtraction.

will be *free* of the possible companion's flux, at least in one of the sets. But we can also use a a full limit displacement of one FWHM instead of one HWHM, to attenuate self-subtraction if required. This condition can be written as:

$$(\frac{\lambda_o}{\lambda_m} - 1)(r + HWHM_{\lambda_m}) \geq FWHM_{\lambda_m} \tag{5.1a}$$

$$(1 - \frac{\lambda_i}{\lambda_m})(r + HWHM_{\lambda_m}) \geq FWHM_{\lambda_m} \tag{5.1b}$$

$$r \geq 138\text{mas} \tag{5.2}$$

If we equal eq. 5.1a and eq. 5.1b, we obtain the spectral channel $\lambda^*_m = \frac{\lambda_i + \lambda_o}{2} = 1.948\mu m$, which is the channel where the radial shift of the PSF features is equal in the outer and inner spectral planes. The PSF in the spectral plane λ^*_m can be modelled by both the outer and inner spectral planes with a maximum radial shift. Replacing this in eq. 5.1a and eq. 5.1b give us a lower limit for the minimum radius that can be reduced by l-SDI (eq. 5.2). Note that this inner working angle can only be reached in one spectral plane (λ^*_m).

In practice these inner limits cannot be reached, since we need more than just one reference PSF in the the *inner* and *outer* set, ideally 75. So λ_i is larger than $1.437\mu m$ and λ_o shorter than $2.460\mu m$. Besides, in SINFONI data, the optimal channel $\lambda_m = \lambda_o + \lambda_i/2$ lies between the two spectral windows H and K.

5.4 Characterisation and Detectability of faint companions

It is important to have both the *inner* and the *outer* sets. Otherwise, when modelling the PSF for a specific annulus, we will not be able to tell if we are incorporating faint companions from the reference annular regions. This is known as selfsubtraction.

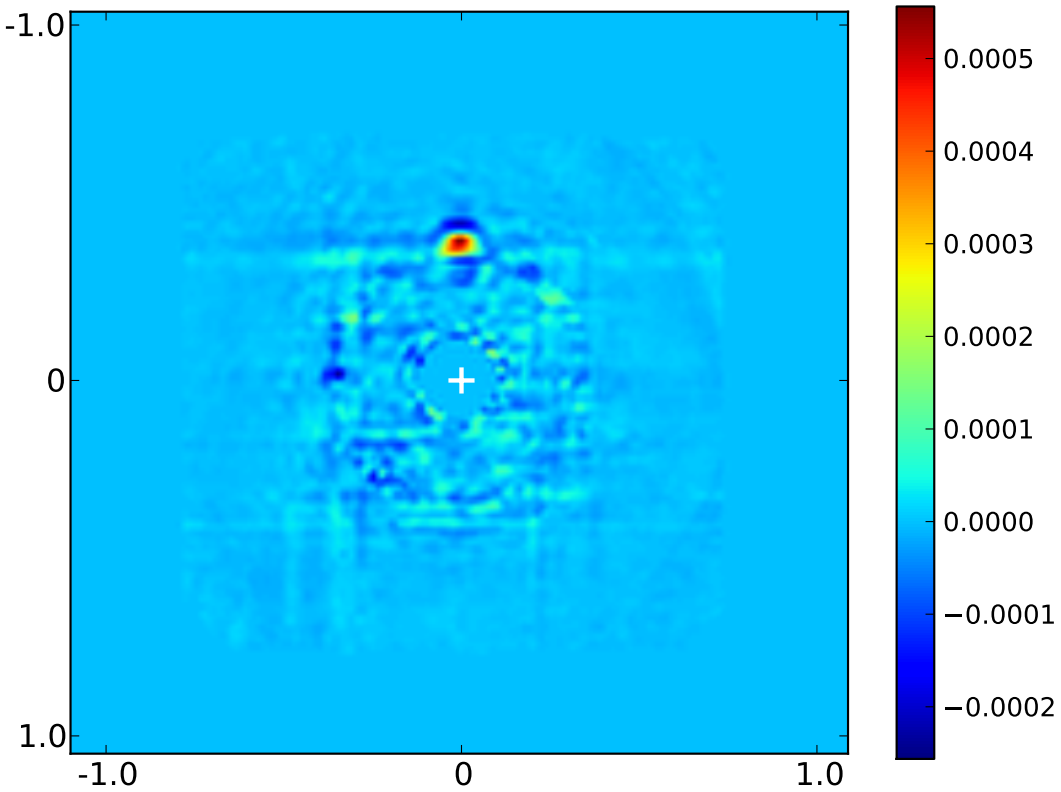

Figure 5.6: Channel 700 at $\sim 1.8\mu m$, showing all annulus regions after the l-SDI was applied, the masked regions are not eligible to be modelled at this channel, because there were no PSFs of reference that matched the selection criterion.

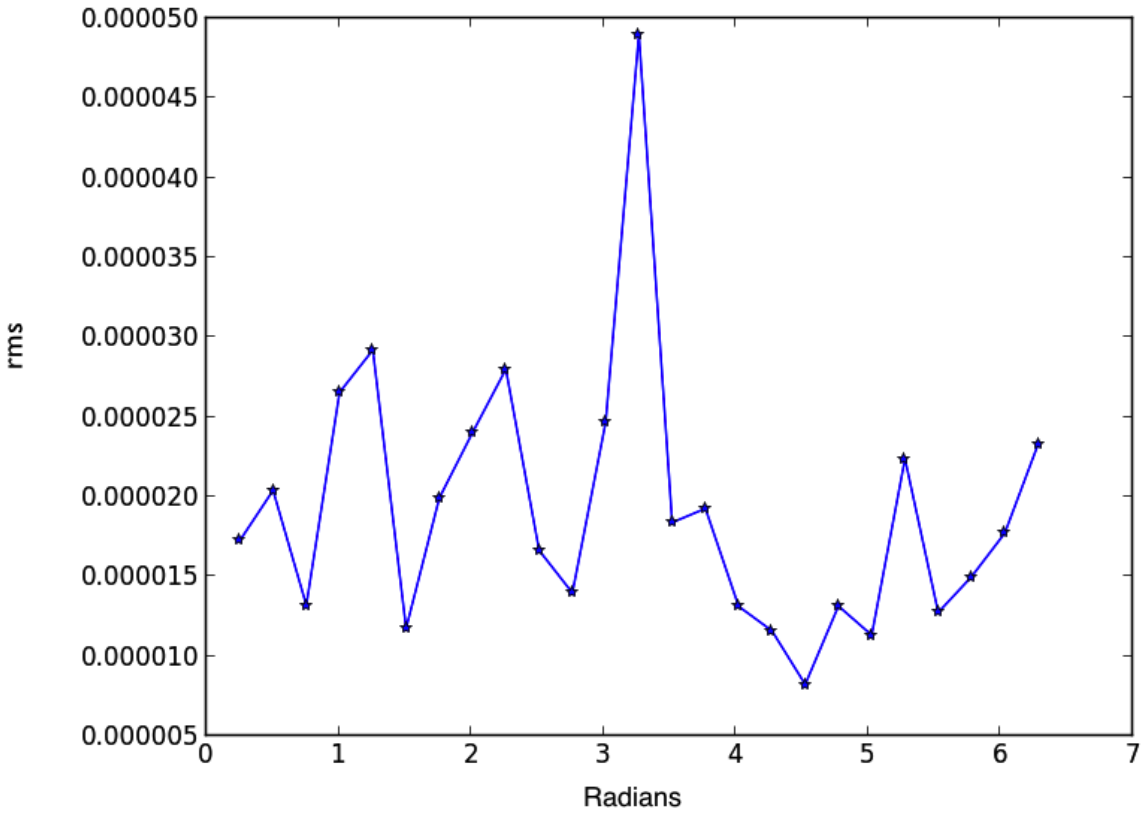

Figure 5.7: Root mean square of 15 segments in the annular regions, the radial width of the regions is roughly two times the diffraction limit. The peak shows the planet signal.

We can see this effect clearly in Fig. 5.6, this is the resulting image after applying the l-SDI techinique to a spectral plane, we can see the detection of a fake companion with a contrast of 5 magnitudes, and at a separation of 37 mas. However we can also see a *negative* of the detection in the inner adjacent annular region.

This happens because when choosing the sets of PSFs to the inner adjacent annular region, we take into account a region with our companion candidate, so the first principal components will replicate it and will inject a negative bias when subtracting the model PSF. To prevent this we could discriminate between the two sets and realise which one has a possible companion. We did not investigate this issue further.

From the angular rms shown in Fig. 5.7, we can easily distinguish the signal as a possible companion. In this way we can establish an n-σ detection criterion for the detectability of candidate companions in one ring. In fact the selfsubtraction effect will aid to detect a signal by this method.

The output of the l-SDI algorithm will be a residual cube with partial spectral data in each spatial pixel, limited by the spatial coverage required to build a PSF in each annular region. To characterise the response of the l-SDI technique we used the fake companions introduced in Fig. 4.1, with different contrast magnitudes. Fig. 5.8 shows the throughput, i.e. the peak from the companion in the residual image (subtracted by the residuals without the fake companion to avoid the effect of bias in noise as in Fig. 5.2) divided by the peak of the input planet in each wavelength. The throughput increases as the flux decreases since PCA will pick-up less of it, therefore subtracting less companion flux.

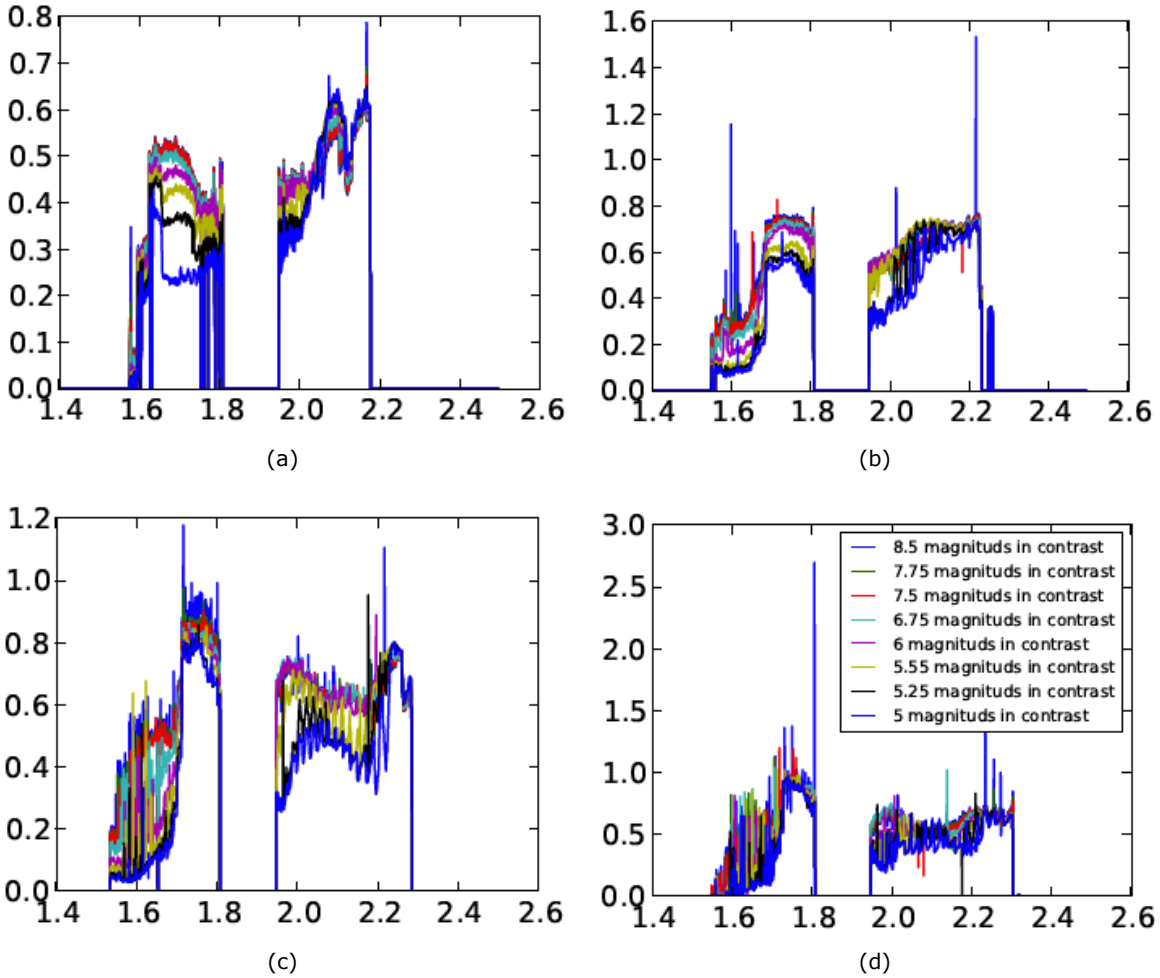

Figure 5.8: Each plot shows the throughput of a companion at 0.251''(Fig. 5.8(a)), 0.375''(Fig. 5.8(b)), 0.500''(Fig. 5.8(c)) and 0.625''(Fig. 5.8(d)). These plots were constructed taking the ratio between the maximum of the fake companion signal at each radius (see Fig. 4.1) and the maximum of the output signal in the resulting cube.

Chapter 6

Results

6.1 Targets

1. *HD 100546:* HD 100546 is an isolated Herbig Be Star (Spectral type B9Ve) of 2.4 $M_{\odot}$, about 27$L_{\odot}$, $T \sim$ 10.500K [Vieira et al., 1999] and an inclination angle of $\sim 40^{o}$. Herbig Ae/Be Stars are pre-main sequence stars (young stars <10Myr) or YSOs (Young Stellar objects), of spectral types A or B. They are usually embedded in star formation regions. HD 100546 has been studied many times by several authors because of its proximity to the earth (103pc) [van den Ancker et al., 1997]. Its large disk enveloping the star has also been studied, first in the NIR with ADONIS on the ESO 3.6m in La Silla [Pantin et al., 2000]. Later it was confirmed that the disk extend over 500AU in radius [Leinert et al., 2004; Liu et al., 2003]. The disk has M$\sim 5 \times 10^{-4} M_{\odot}$ assuming 50K of dust temperature [Henning et al., 1998]. It has been suggested that the disk presents a cavity (empty region or gap) somewhere within 10 AU [Benisty et al., 2010; Bouwman et al., 2003; Panić et al., 2010; Tatulli et al., 2011]. A companion candidate has been recently reported by Quanz et al. [2013b] in L' band using ADI.

2. *HD 142527:* The star HD 142527 is a Herbig star, spectral type F6 IIIe [Houk, 1978; Waelkens et al., 1996]. The distance calculated by the parallax value from the Hipparcos catalog is $d = 233^{+69}_{-43}$ pc [van Leeuwen, 2007], but the star has been identified as member of the star forming region Sco OB2-2 [Acke and van den Ancker, 2004] or the Upper Centaurus Lupus [de Zeeuw et al., 1999] and the distance by that association would be $d = 145 \pm 15$ pc. Recent SED modelling and VISIR imaging suggests a disk gap from 30 - 130 AU, an age of $\sim 5Myr$ and stellar mass of $M = 2 \pm 0.3 M_{\odot}$[Verhoeff et al., 2011]. The outer edge of the gap as well as a spiral feature in the outer disk have been imaged in the near-IR and it was found that the star center has an offset of 20 AU to the disk center presumably caused by a companion [Fukagawa et al., 2006]. Biller et al. [2012], reports a likely close companion at 88 mas (12.8 AU at 145 pc) of 0.1-0.4 $M_{\odot}$, but this scenario with one single companion, does not prove to be effective for clearing this large gap in a FARGO simulation leaving a wider inner disk. Additional close-in companions maybe required to deplete the entire region [Casassus et al., 2012]. Recently, filaments in HCO+ and CO gas were found inside the gap that support the accretion rate of the inner disk to the star [Casassus et al., 2013].

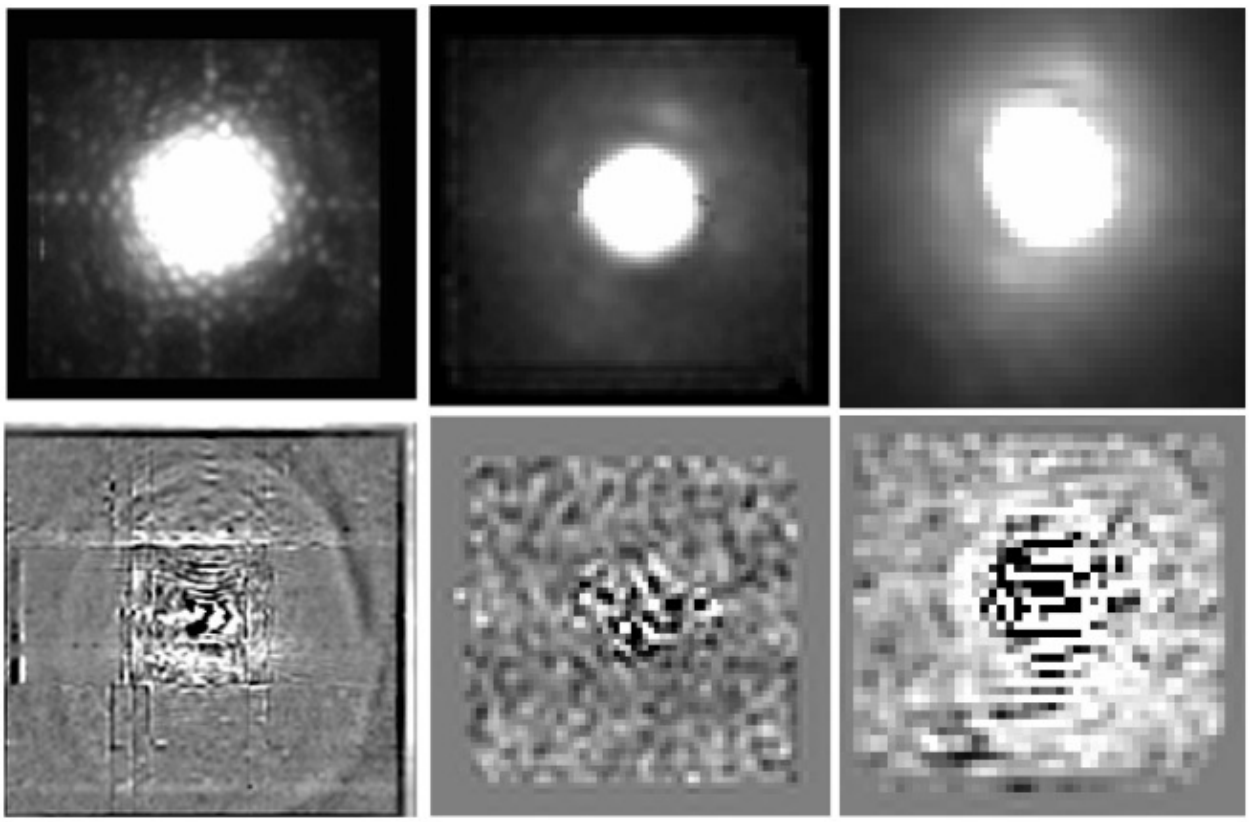

Figure 6.1: From left to right , HD 142527, T_ cha, HD 100546. The upper images correspond to a channel of the original data around 2.1μm, and the lower ones correspond to the residual channel after applying SDI.

3. *T Cha:* Is a weak-lined T Tauri star with a mass of $1.5 \sim M_{\odot}$ [Alcala et al., 1993], and belongs to the association ϵ Cha that is 108 $\pm$9 pc away [Torres et al., 2008]. Its age, according to a study of the ϵ Cha association, is around 5-10 Myrs [da Silva et al., 2009]. Its SED suggest an optically thick inner disk within a larger inner hole [Espaillat et al., 2010; Olofsson et al., 2011]. A companion candidate has been recently detected in L-band, at 6.7 AU [Huélamo et al., 2011] using SAM.

6.2 Results of SDI and l-SDI

The SDI technique was applied to HD 142527, HD 100546, and T Cha firstly without the radial optimization (see Fig.6.1) as well as the polynomial fit algorithm. From HD 142527 the inner rim of the outer disk is easily distinguishable. The FoV of HD 100546 and T Cha (0.8"x0.8") is considerable smaller than the mosaic of HD 142527 ($\sim$1.6"x1.6"). HD 100546 does not have a prominent gap and the disk is really large (500AU). The companion candidate of HD100546 lies out of our FoV by a few arcseconds. As for the companion reported in Huélamo et al. [2011], its too close to the star (67mas), where l-SDI cannot construct a PSF. Besides Huélamo et al. [2011] reported no detection in the Ks band, having only detected the signal in the L' band.

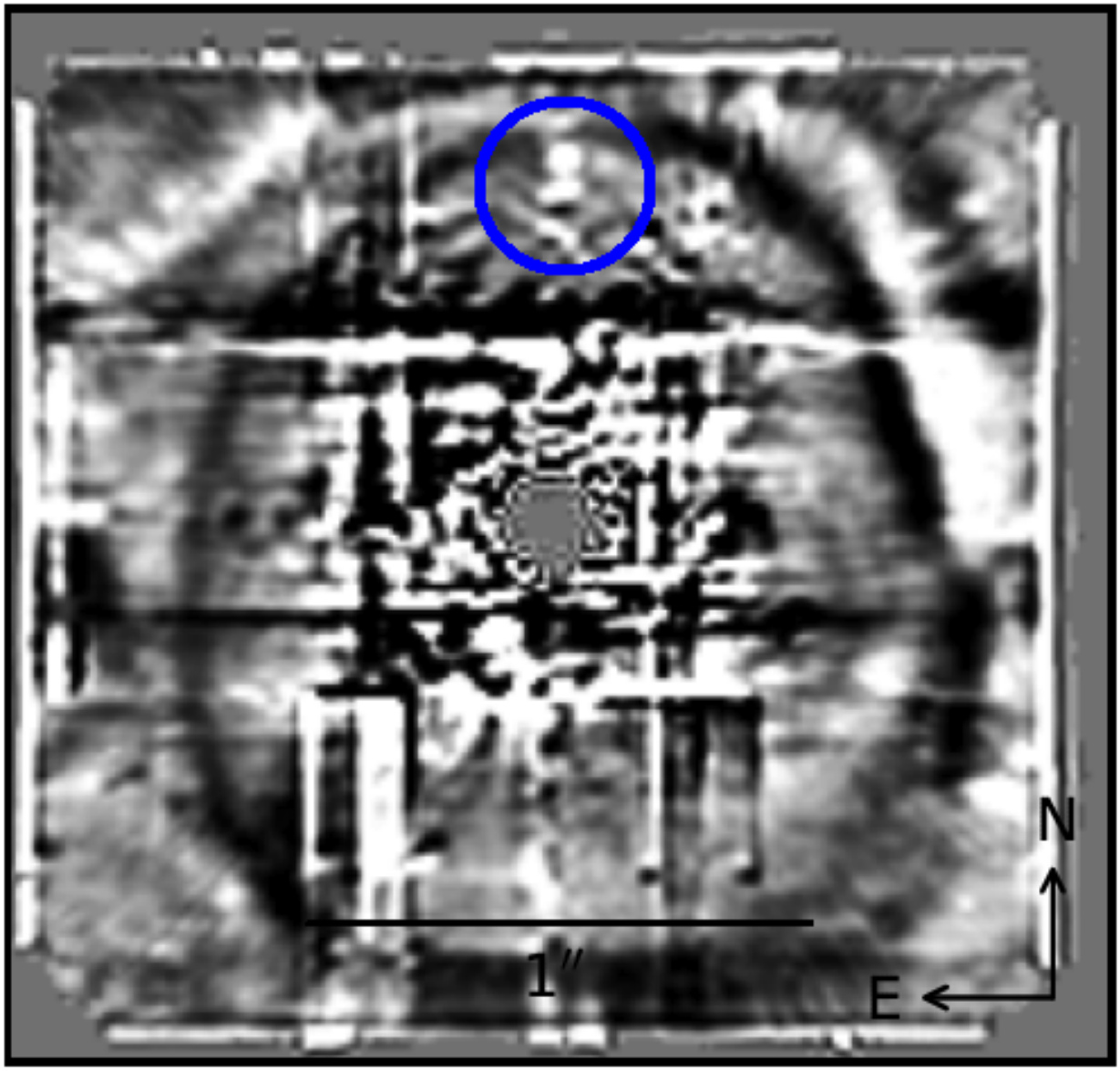

Figure 6.2: Collapsed image of the entire residual cube, showing bright vertical and horizontal features. At 0.73" a bright point-like source can be seen. The star shows an offset to the center of the disk. A spiral-like structure is seen to the north-east, that has not been seen in before.

6.3 Spiral-arm-like structure and companion candidate

The l-SDI algorithm was applied to the HD 142527 data and we show in Fig.6.2 a collapsed cube to improve contrast, which is the median of all spectral planes containing residual signal. We can easily distinguish vertical and horizontal features that are produced by the combination algorithm to create the mosaic.

We cannot see the spiral arm reported by Fukagawa et al. [2006] because it is out of our FoV. The morphology of the disk at the east suggests the beginning of a spiral-arm structure to the north-east that has not been reported, and that it is not visible in the NICI observations from Casassus et al. [2013]. This new feature could be the opposed arm of that seen in the south-west by other NIR images [Canovas et al., 2013; Fukagawa et al., 2006]. A comparison of this data with other NIR images is discussed in Sec. 7.3.

We report a $\sim 3\sigma$ ($S/N = 3.5\sigma$, taking the ratio between the peak of the signal in the collapsed cube and the standard deviation) detection of a point source at an angular separation of 0.738'' almost straight to the north, that is completely hidden in the noise in the collapsed cubes of the polynomial fit algorithm and the PCA algorithm with no radial optimization ($S/N = 1.79\sigma$ and $S/N = 1.365\sigma$, respectively).

In Fig.6.7, we show the spectra of the candidate companion in K-band, along with the spectra of the host star, a fake companion with a flat input spectra, a hotspot in the residual image nearby the companion candidate, a bright mosaic feature nearby the companion candidate, and a region of the disk to the west of the host star. The companion candidate spectra shows a tendency of a maximum towards longer wavelength, unlike the star that shows clearly a negative spectral index, the same as the mosaic feature. The hotspot shows a local maximum but is generally flat, the disk shows more dispersion but no clear spectral index. All the spectra were extracted by summing boxes and are corrected by the throughput of a fake companion at 0.62'' with a contrast magnitude of $\Delta m = 8.5$. We can't provide a H-band spectra because there was no PSF estimate in the spatial region of the companion candidate due to the shrinking of the cube.

The companion candidate has an absolute magnitude of $M_K = 13.1$ in the K band (corrected by the same throughput as the one mentioned above). Gemini NICI observations of this source were imaged [Casassus et al., 2013], and for an absolute magnitude of 13.1 at an angular separation 0.738'' the upper limits cannot certainly rule out the companion. We show in Fig.6.4 a detection limit curve and the contrast magnitude of the companion candidate. The curve is corrected by a throughput that was interpolated radially with the actual throughput of our four fake companions with $\Delta m = 8.5$ at 0.251'', 0.375'', 0.500'' and 0.625'' of angular separation.

We apply the l-SDI techinque to the remaining 25 mas spatial resolution data of HD142526, using only the tiles where the companion candidate is located. It appears clearly in the north tile of the two observations sets from 2012, but it does not appear in the tiles of the set of observations of 2013 as we can see in Fig.6.5, so no detection can be claimed.

We applied l-SDI to the 100 mas spatial resolution data of HD 142527 (see Table 4.1). We get a residual cube that contains most of the features of the previous set of 25 mas, but the faint spiral arm at the north-east is not clearly visible. We present a collapsed cube, taking the median of all spectral planes where residuals are present, of the relevant disk structure in K-band (see Fig. 6.6).

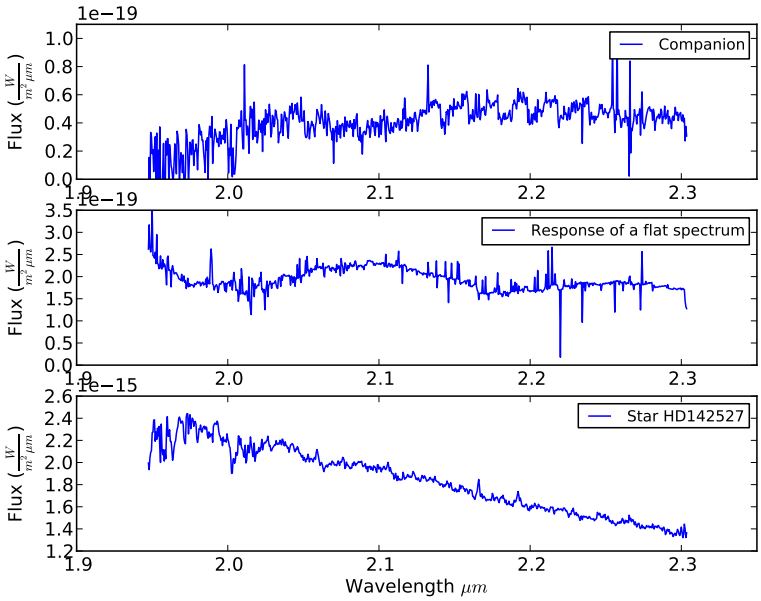

(a)

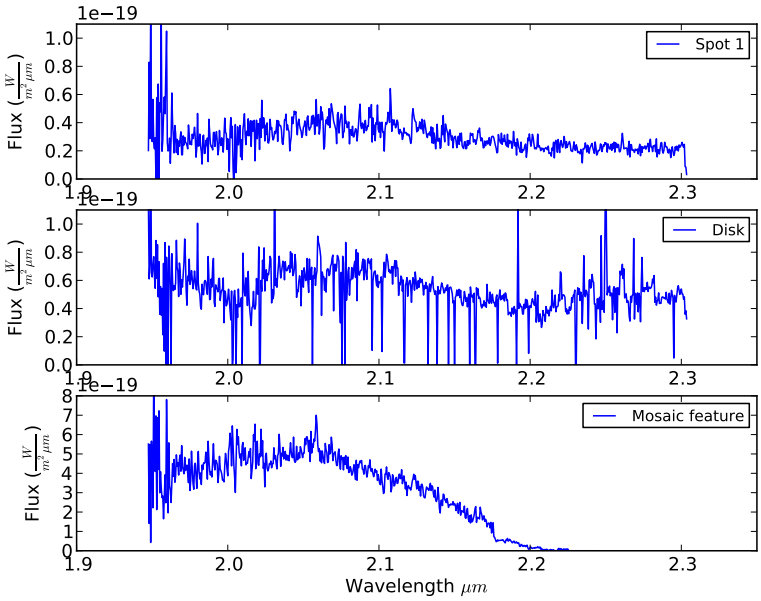

(b)

Figure 6.3: On the top panels we show spectra from the companion candidate, the host star HD 142527, and a fake companion with a flat input at 0.73''. On the bottom panels we show the spectra from a bright source in the residual image close to the companion candidate, a bright region of the disk west to the host star, and a mosaic residual feature, close to the companion candidate.

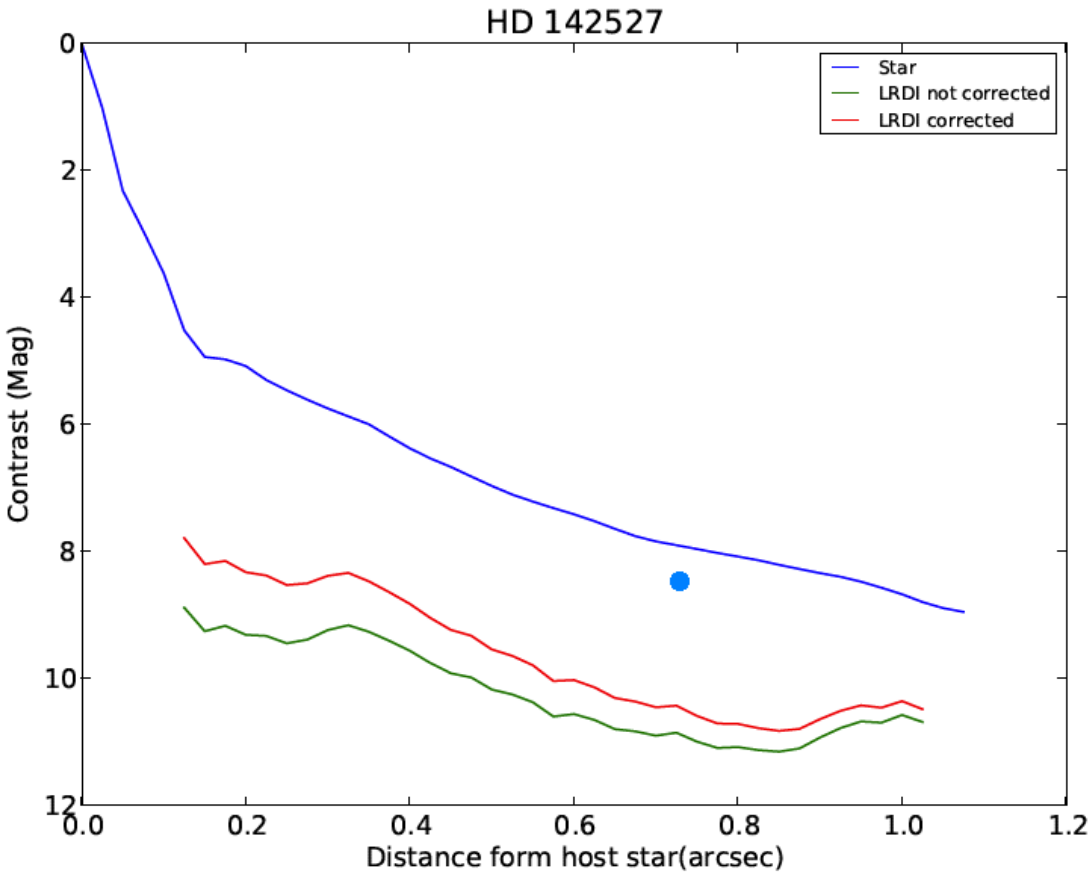

Figure 6.4: Solid blue line correspond to a radial profile of the star, the red line is a 3-σ detection level corrected by the throughput, and the green light is the uncorrected limit. The blue dot represents the companion candidate at 0.73". The standard deviation was calculated as the mean of the rms in equally-spaced annular regions in a ring at each radius. The throughput used was interpolated from Fig.7.1.

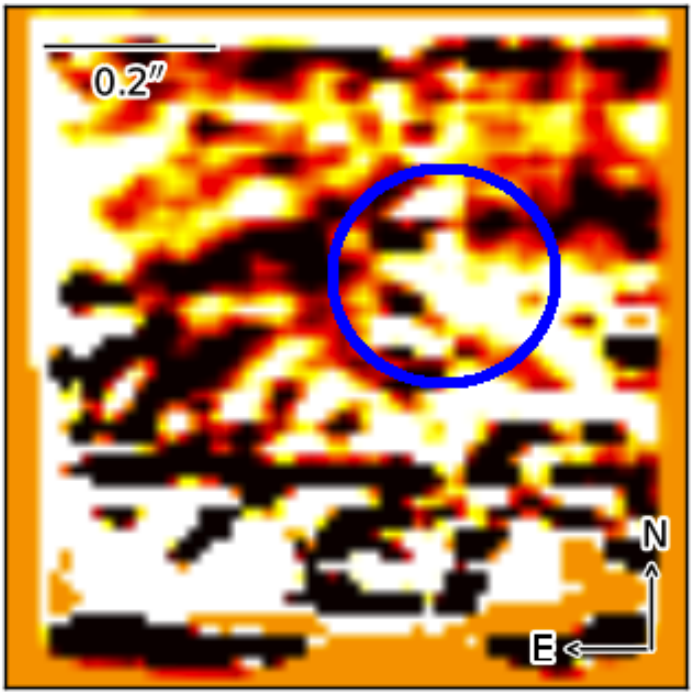

(a)

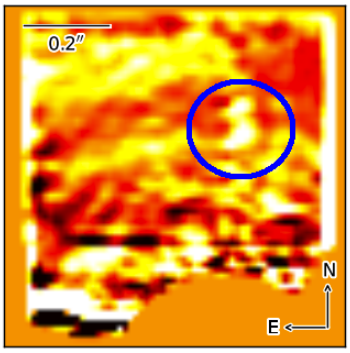

(b)

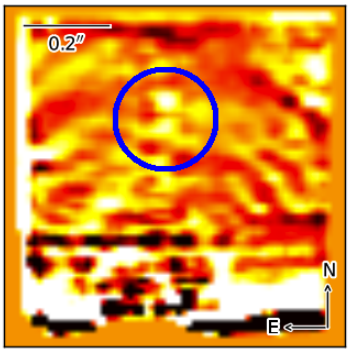

(c)

Figure 6.5: The bottom figures 6.5(b) and 6.5(c), correspond to collapsed images after applying l-SDI. They only show the north tiles of observations taken in 2012 (no mosaic) in H+K band, where the point-like signal can be seen. The upper figure 6.5(a), show a collapsed image after l-SDI of the north tile of one observation of 2013 in H+K band, showing no signal. The other observation of 2013 does not cover the position of the companion candidate.

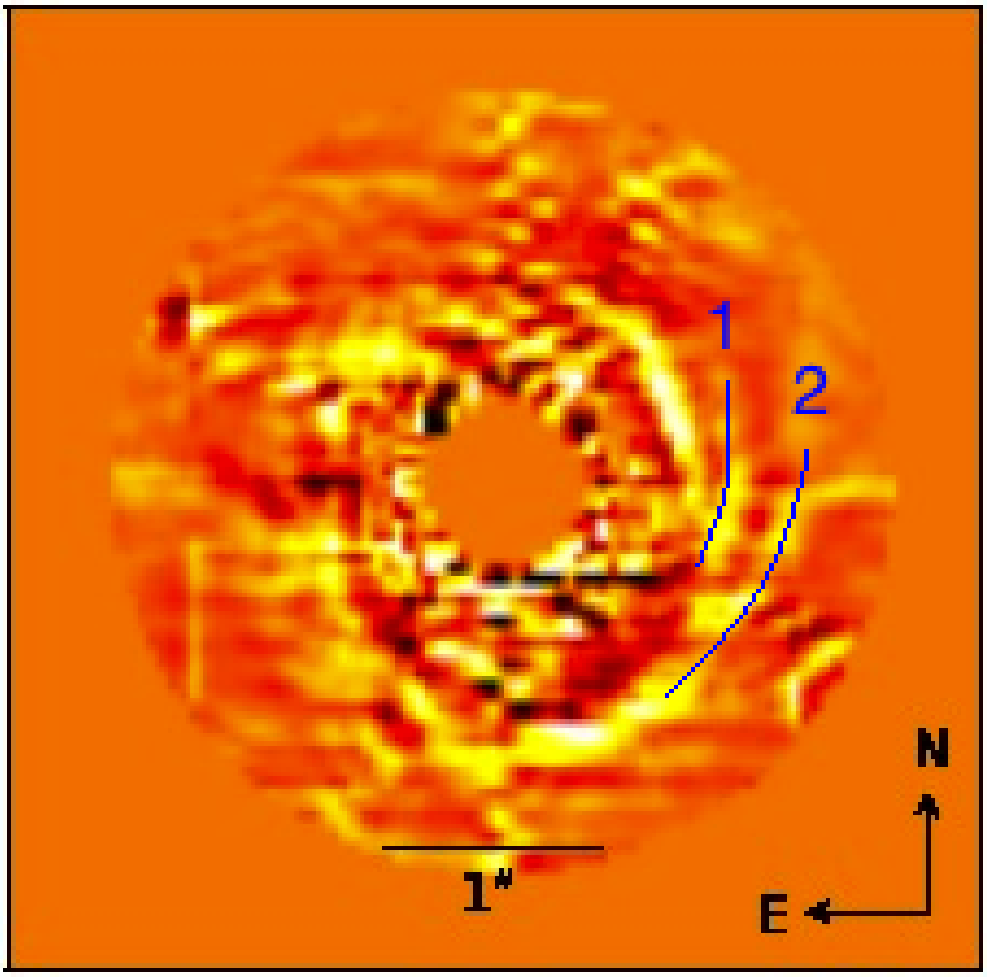

Figure 6.6: Collapsed image of the entire residual cube of 100 mas, in K-band. Two spiral arms (1 and 2) can be seen that resemble previous NIR observations [Canovas et al., 2013; Casassus et al., 2012, e.g.].

6.4 HD 100546 and T Cha

Both this sources have companion candidates in the literature. Huélamo et al. [2011] reported a source in L' band at 65 mas of angular separation, P.A. of $\sim 78 \pm 1$ degrees, and Quanz et al. [2013a] reported a source at 0.48" ~ 0.04" of angular separation, P.A of 8.9 ± 0.9 degrees.

Unfortunately our observations of T Cha and HD 100546 have a small FoV (0.8"x0.8"), so the companion for HD 100546 will be out of the FoV. The companion candidate in T Cha is too close to the star, where l-SDI cannot be fully applied.

Nevertheless it is possible to apply l-SDI partially, but the S/N will be lower since we have fewer reference PSFs that match the radial selection criterion. We get detection limit curves for possible companions corrected by its correspondent throughput for HD 100546 in Fig. 6.7(a) and T Cha in Fig.6.7(b) .

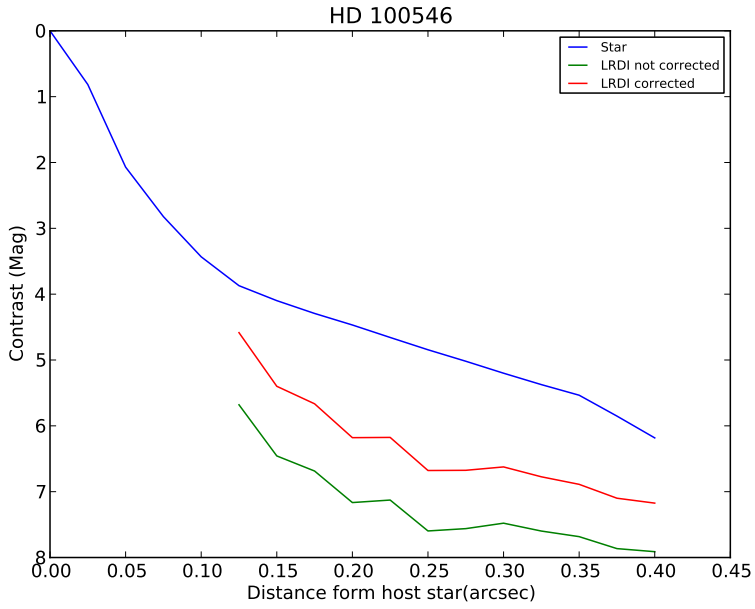

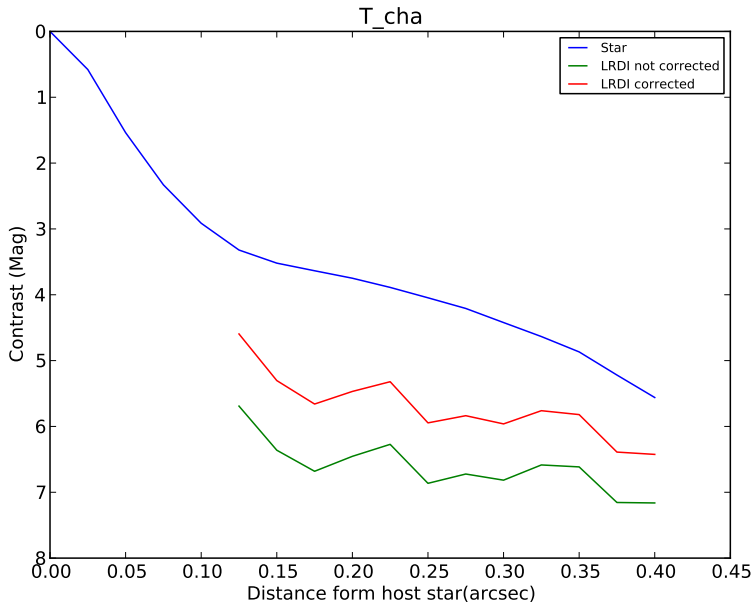

Figure 6.7: Contrast limit curves of HD 100546 and T Cha, both corrected by throughput, the curves represent a 3-σ detection, and σ was calculated as the mean of the rms in equally-spaced annular regions in a ring at each radius.

Chapter 7

Discussion

7.1 The PSF model

l-SDI presents an alternative way to create a PSF model. LOCI uses the same principle in choosing the PSF reference stack, but it uses a localized optimization based on leasts squares, while l-SDI uses a principal component regression. This multiple regression presents multicollinearity, i.e the least square fit gives coefficients that have high covariance. If we slightly variate our set of data to estimate the coefficients, then we will see an erratic change in the coefficients due to the high correlation existing in our stack of PSFs. This multicollinearity can be resolved, for example, using less coefficients estimators, but choosing them is a difficult task. PCA provides a set of uncorrelated stack of reference PSFs that do not have this problem, unless we use all of its components. Akaike's information criterion allows to discriminate how many of them are need. However PCA coefficient calculation seem to be more stable than least square methods [Flury and Riedwyl, 1988, p.212].

l-SDI subtract less input flux on fake companions than a non-localized PC regression, as we can see from Fig.7.1 compared to Fig.5.2 we get roughly twice the amount of throughput for each input flux with a localized treatment. And we see as well a peak of sensitivity at $\sim 0.25''$, that could be due to the biased number of reference PSFs we get for each region and channel, i.e. we get less coverage for the outer and inner regions with a limited wavelength coverage.

7.2 The characterization of throughput and the detectability criterion

As we explained in the sections above, to fully characterize l-SDI, we need to measure how much flux of the companion candidate is recovered after l-SDI is applied, i.e. we need to determine the throughput. We calculate the throughput as the ratio of the peak in both the residual and the original image. This first approximation assumes that the PSF of the companion is preserved during l-SDI, which is clearly not the case, since there is always some degree of selfsubtraction.

To better characterize l-SDI, one should perform and statistical analysis to determine the true output flux. Consider a companion (fake or not) at given approximate position in the FoV. Prior to l-SDI, one could inject a *negative* at different positions and fluxes in a grid where the

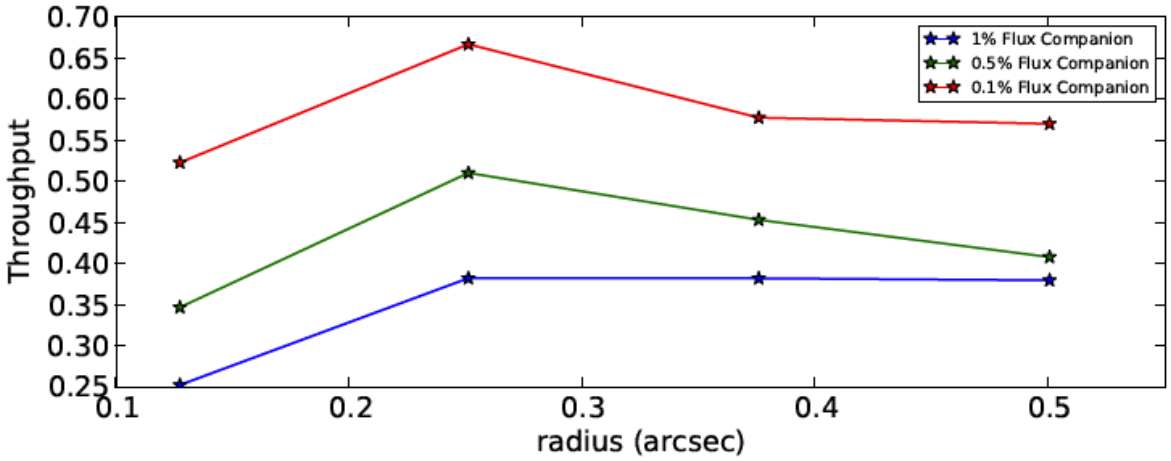

Figure 7.1: Throughput for l-SDI. It was constructed in the same way as Fig.5.2, but we do take the mean of all spectral planes excluding those regions where the PSF cannot be estimated.

companion is known to be placed. Then apply l-SDI to each of this simulated images with fake *negative* companions. We can compute a measure of the variance similar to a χ^2 distribution as

$$V(F,\vec{x}) = \sum_{ji} \frac{\mathrm{R}_{ji}(F,\vec{x})^2}{\sigma^2}, \tag{7.1}$$

Where F is the input flux of the *negative* companion and $\vec{x}$ its position, $\mathrm{R}_{ji}(F,\vec{x})$ is the value of the $[j,i]$ pixel ($[j,i]$ ϵ grid) on the residual image (with an injected fake *negative* companion) after l-SDI, and σ its intrinsic error, estimated from the rms of a nearby region.

A minimum in Eq. 7.1 will give us a good estimate on the true flux and position of the companion candidate and can be used as detectability criterion if we calculate the error on the estimated flux. Applying this one can also construct a throughput that will be not limited by the conservation of the PSF parameters after l-SDI.

7.3 Comparison with other NIR imaging

HD 142527 has been imaged in the infrared before. The morphology of this disk has been studied by Ohashi [2008], Verhoeff et al. [2011] and Fujiwara et al. [2006] in Mid-IR. Its internal structure has been modelled from the SED by Verhoeff et al. [2011]. Its complicated structure is not fully described by simple models, and suggests a perturbed state, presumably by a possible companion opening a gap by dynamical clearing [Bryden et al., 1999], or a binary system [Fukagawa et al., 2006], although no evidence of a binary companion has been reported. Observations of more transition disks with companion candidates will hopefully clarify how this state is reached.

Polarised imaging of this disk has been recently reported by Canovas et al. [2013] and it is consistent with our observations. NICI imaging with ADI reported by Casassus et al. [2012] shows 4 arm structures, three of which can be seen in our mosaic image (see Fig.7.2 numbers 1, 2 and 3). We confirm the shift of the west arm seen by Rameau et al. [2012] in L' band and by Casassus et al. [2012] (see feature 5 in Fig.7.2), that can correspond to the beginning of

Fukagawa's arm. We also see the east arm fainter than the west arm (see Fig.7.2 number 1 represents the east arm, and number 2 the west arm). This so-called arms are nothing but the inner rim of the outer disk.

We report a new spiral arm structure that can be seen from P.A 22^o to P.A 68^o that has not been seen before (number 4 in Fig.7.2), probably a counter part of a southern-west spiral-arm seen in ALMA band 7 data (Christiaens et al. 2013, in prep). We do not see this structure at a lower spatial resolution in Fig. 6.6, but we have a better image of the disk free from mosaic artefacts.

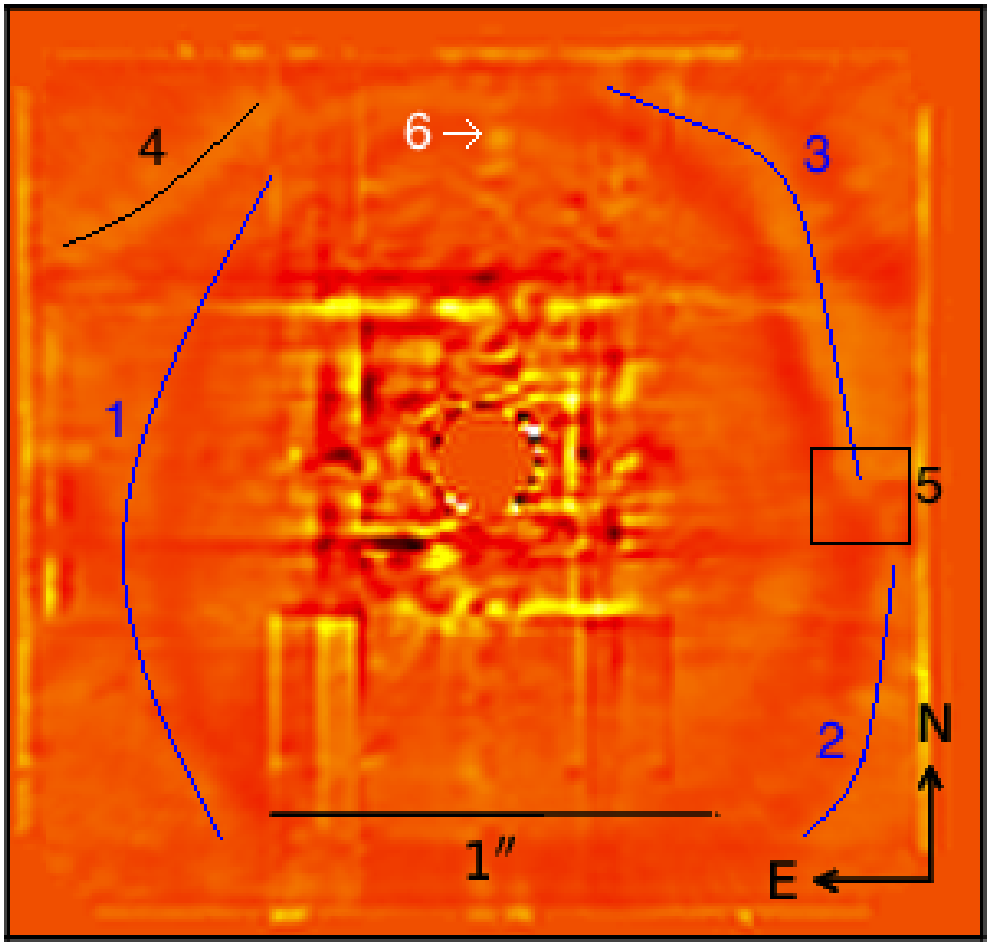

Figure 7.2: The blue lines are structure already reported, the black box shows the region where the discontinuity of the west arm is located, and the black line shows the new spiral-arm. The white arrow shows the location of a possible companion.

Chapter 8

Conclusions

In this thesis we have provided a new algorithm (l-SDI) that improves previous attempts of SDI by constructing a PSF radially localized with less contamination by a possible companion, thus increasing roughly twice the amount of flux throughput compared to its non-localized version. We have tested our technique with SINFONI observations mainly in the transition disk of HD 142527. It is important to notice that in order for the technique to work we need a wide coverage in wavelength, since it is essential to get enough radial displacement of features to construct the PSF in a wide range of angular separations. K-band observations prove to be not sufficient as H+K bands observation, only a narrow range of angular separations were suitable to construct a PSF in all the wavelengths channels.

A few weeks before this thesis was finished Oppenheimer et al. [2013] reported the extracted spectra of all four companions of HR8799 with a technique very similar to l-SDI called S4. They do not show the details of this technique but the overall view seems very alike. They used the same selection criterion to choose the reference PSFs, and they also model the PSF through a principal component regression.

We report a new NIR image of the surrounding disk of HD 142527, confirming previous spiral-arm structures,a new spiral-arm structure and a possible companion at 0.73'' with a contrast magnitude of M_K $\sim$13.1 that need to be followed up. This new algorithm allows to improve high-contrast observations with IFSs, and will be helpful with new instruments aimed to the detection of faint companions such as SPHERE. A further work in the characterisation of the response of extended emission is needed. An effective way to find the center of the PSF is needed to apply the algorithm to observation where the center of the star is not in the FoV, thus the observation can be localized only towards the region of interest.

A full characterisation of the l-SDI technique is needed by a more robust measurement of the throughput as explained in 7.2. A characterisation to the response of extended emission is also needed. To test this response, the simplest way is to use a model of a well studied disk such as HD 100546 to be tested with the l-SDI technique. Using Lime radiative transfer code, and a model from the literature (e.g. Benisty et al. [2010]), a data cube can be constructed and compared to the residuals obtained by the real data .

Appendix A

In that case, we can estimate the center of the star by two different ways:

1. *Gradient estimate:* The PSF will roughly have a gradient towards the center of the PSF. So we can get an estimate of the center, by intersecting the gradient vector field of the image between all the available points (a sobel filter can be used to get the gradient vector field), and then take a median from all the intersection values. This method works better if we, somehow, empirically know the approximated center of the PSF. Because we can put a constrain on the intersection values that are close to the center, eliminating from the sample those intersections that are produced by irregular features of the PSF (e.g. blobs, speckles).

2. *PSF wavelength dependence:* We can get a numerical derivative of the PSF by subtracting spectral planes of the partial FoV. If we can get an algebraic expression with explicit dependence in wavelength, then solving for the center of the PSF is straightforward. But getting such an expression is complicated because the Moffat and Gaussian profiles, that could provide acceptable fits to the PSF, do not have explicit dependences in wavelength. Airy patterns are more difficult to use since they involve Bessel functions and so they must be solved numerically .

The Gradient estimate is a good first approximation if we don't have the star in the FoV.

Appendix B

In this appendix Principal Component Analysis(PCA) is briefly described, and some general notions regarding principal component regression are discussed.

.1 Definition

Principal Components are a linear transformation of a set of random variables that are uncorrelated between each other, and are orderer in increasing variance.

Let's consider a vector $\vec{x}$ of p random variables, and the function

$$f(\vec{x}) = \vec{\alpha_1}^T \vec{x}, \tag{1}$$

a linear combination of coefficients $\alpha_{11}, \alpha_{12}, \cdots, \alpha_{1p}$. We seek first, that the variance of this function is maximized. The $\vec{\alpha_1}$ vector is then determined by maximizing its variance $var[\vec{\alpha_1}^T \vec{x}] = \vec{\alpha_1}^T \Sigma \vec{\alpha_1}$, where Σ the variance-covariance matrix of the vector $\vec{x}$. To maximize it we clearly need a (normalization) constrain on the coefficients $\vec{\alpha_1}^T \vec{\alpha_1} = 1$, using Lagrange multipliers we have that

$$\vec{\alpha_1}^T \Sigma \vec{\alpha_1} - \lambda(\vec{\alpha_1}^T \vec{\alpha_1} - 1) = 0, \tag{2a}$$

or

$$(\Sigma - \lambda \mathtt{I}_p)\vec{\alpha_1} = 0 \tag{2b}$$

λ is an eigenvalue of Σ, and we need to maximize,

$$\vec{\alpha_1}^T \Sigma \vec{\alpha_1} = \vec{\alpha_1}^T \lambda \vec{\alpha_1} = \lambda \vec{\alpha_1}^T \vec{\alpha_1} = \lambda, \tag{2c}$$

So the variance is maximized with the largest egienvector $\vec{\alpha_1}$ of Σ.

Calculating the eigenvectors and eigenvalues of Σ, will allow us to construct the first Principal Component (PC) of the sample, with the largest eigenvalue and its eigenvector $(\lambda_1, \vec{\alpha_1})$. We then take the second largest eigenvalue and its correspondent eigenvector $(\lambda_2, \vec{\alpha_2})$ to construct the second PC and so on.

To visualize it, we can think of the easiest example $p = 2$. A set of vectors of random variables could represent a highly correlated group of points in the Cartesian plane (x_1, x_2). The PC transform of such a sample, will get its mayor variance and the second largest variance in two orthogonal vectors defining a new Cartesian plane (z_1, z_2)(see Fig.1).

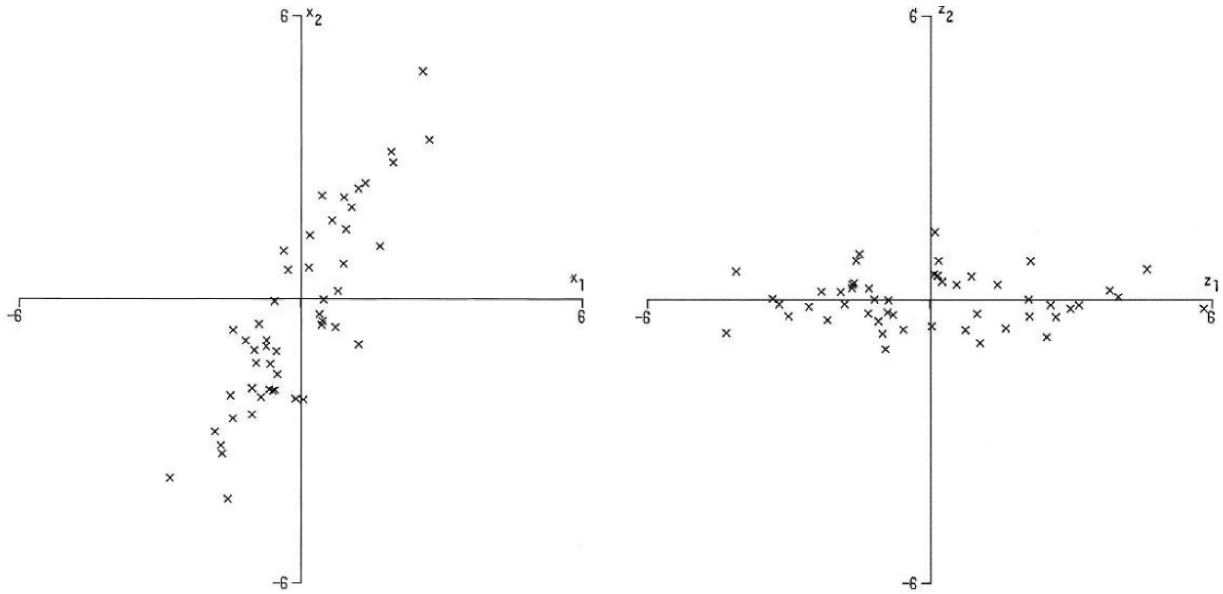

Figure 1:

.2 Application to SDI problem

Our case is very similar to the one above, but we have a vector of random vectors instead (i.e. a matrix). We use a singular value decomposition [Jolliffe, 2002, p.44] of a matrix S, whose rows are vectorised versions of the PSF data in each channel. This will give us three matrices, U, M, and V, such that

$$\mathbf{S} = \mathbf{UMV}^T, \tag{3}$$

where **M** is a diagonal matrix containing the singular values of Σ the sample covariance matrix of **S**, and **V** is a matrix that contains the vectorised principal components. The components are sorted in decreasing variance of its singular values, that are the square root of the eigenvalues of the sample covariance matrix Σ, being the first principal component the one that accounts for the largest variance (i.e the largest singular value).

Of the 2172 channels originally available in the SINFONI data, we use only 700 after avoiding bad channels in the wings of the H and K bands. We thus reduce the operational time of the SVD decomposition. There is a way to weight PCA but the basis will not be orthogonal which is exactly what we are looking for [Kriegel et al., 2008]. If we model the PSF with an orthogonal basis, we will get rid of the multicollinearity problem, which is addressed below in Sec. 7.1.

Since the PCA decomposition gives us an orthonormal basis set, it is possible to have a linear combination that describes each vectorised image channel,

$$\vec{I}(\lambda) = \sum_{i=0}^{q} a(\lambda)_i \vec{C}_i, \tag{4a}$$

where the principal components $\vec{C}_i$ are the columns of the **VM** matrix. M is a diagonal matrix of the singular values of Σ, the sample covarience matrix of S.

Thus the $a_i(\lambda)$ coefficients of each image can be easily computed by taking the inner product

of each basis with the image channel [Amara and Quanz, 2012]

$$a_i(\lambda) = \vec{I} \cdot \vec{C}_i, \tag{4b}$$

since the inner product of the principal components is the Kroenecker delta by definition

$$\vec{C}_j \cdot \vec{C}_i = \sum \vec{C}_i \vec{C}_j = \delta_{ij}, \tag{5}$$

using eq. 5 in eq. 4a gives eq. 4b.

Appendix C

Wax and Kailath [1985] used AIC to determine the number of independent signals in their model, without empirically setting the number of PCs to be used.This number is determined by the minimization of the AIC criterion. The determination of the number of independent signals to be used in SDI or l-SDI , reduces to determine the number of principal components to be used in modelling the PSF (entirely or partially, whether if SDI or l-SDI is applied).

We proceed as exactly as Wax and Kailath [1985] did but with our vectorised images. The following is the recipe as shown in their paper:

We first vectorise each spectral plane and regard them as a set of observation vectors $\vec{I}(\lambda)$ of length p, drawn from some probability distribution. The length of $\vec{I}$ is determined by the amount of spatial pixels in an image plane at a given wavelength We would like to have a basis set that can model this data as follows:

$$\vec{I}(\lambda) = \sum_{i=0}^{q} a_i(\lambda)\vec{C}_i + r(\lambda), \tag{6a}$$

where $\vec{C}_i$ are the principal components of the sample,

$$a_i(\lambda) = \vec{C}_i \cdot \vec{I}(\lambda)^{\mathbf{T}} \tag{6b}$$

are the coefficient for each basis, and $r(\lambda)$ is the residual vectorised image that does not contain the PSF of the host star. In this scenario we need to determine the number of PCA, i.e q, such that the inclusion of further principal components does not improve the residuals.

The criterion seeks to find the best model from a family of models. Given a set of observations $\vec{X} = [\vec{I}(\lambda_1), \cdots, \vec{I}(\lambda_n)]$, the family of models will be parametrised by Θ that defines a probability density $f(\vec{X} \mid \Theta)$, i.e. the probability of obtaining the vector $\vec{X}$ with the model parametrised by Θ

Akaike's criterion selects the model which gives a minimum AIC

$$AIC = -2\log f(\vec{X} \mid \hat{\Theta}) + 2m, \tag{7}$$

where $\hat{\Theta}$ is the set of parameters of the model that maximizes the probability $f(\vec{X} \mid \Theta)$, where $\vec{X}$ contains our vectorised observations, and m are the number of free adjusted parameters. That probability is commonly known as the likelihood function $\mathcal{L}(\Theta)$, and the first term of the AIC function as the log-likelihood of the maximum estimator $\hat{\Theta}$.

To calculate the log-likelihood function we regard each of the vectorised spectral planes

as statistically independent Gaussian vectors with zero mean that have a multivariate normal distribution:

$$f(\vec{I}) = \frac{1}{\pi^p \det \mid \Sigma \mid} e^{(\vec{I}-\vec{\mu})^T \Sigma^{-1} (\vec{I}-\vec{\mu})}$$

, where Σ is the covariance matrix of the model.

We previously defined our model as described in equation 6a rewriting it

$$\vec{I}(\lambda) = \mathbf{C}\vec{a}(\lambda) + \vec{r}(\lambda) \tag{8a}$$

where C is a matrix containing the principal components

$$\mathbf{C} = [\vec{C}_\circ, \cdots, \vec{C}_q], \tag{8b}$$

and $\vec{a}(\lambda)$ is a vector containing the coefficients

$$\vec{a}^{\mathbf{T}}(\lambda) = [a_\circ(\lambda), \cdots, a_q(\lambda)]. \tag{8c}$$

So the covariance matrix for this model will be

$$\Sigma = \Phi + \sigma^2 \mathbf{I}, \tag{9a}$$

where

$$\Phi = \mathbf{CAC}^\dagger, \tag{9b}$$

and

$$\mathbf{A} = E[\vec{a} \cdot \vec{a}^\dagger], \tag{9c}$$

where $E[a]$ denotes the expectation value of a.

The rank of Φ in this model is q, equal to the columns of **C**, i.e. the principal components are linearly independent, and the **A** matrix is non-singular. This means that the $p - q$ smallest eigenvalues will all be equal to σ^2. We could just see the eigenvalues of the covariance matrix and determine the number of independent signals q from ordering them decreasingly. But this covariance matrix is unknown in practice, instead we do know the sample covariance matrix Σ_S.

Let's consider a family of covariance matrices

$$\Sigma_k = \Phi_k + \sigma^2 \mathbf{I} \tag{10}$$

where k is its rank. Each of these models will have a set of parameters that represents the covariance matrix,

$$\Theta_k^{\mathbf{T}} = (\lambda_1, \cdots, \lambda_k, \vec{V}_1^{\mathbf{T}}, \cdots, \vec{V}_k^{\mathbf{T}}) \tag{11}$$

Now we can calculate the joint probability density of our family of models.

$$f(\vec{X} \mid \Theta_k) = \prod_{i=0}^{N} \frac{1}{\pi^p \det \mid \Sigma_k \mid} e^{-\vec{x}(\lambda)^\dagger \Sigma_k^{-1} \vec{x}(\lambda)} \tag{12}$$

Taking the logarithm we get the log-likelihood function

$$\mathcal{L}(\Theta_k) = -N\log(\det \mid \sigma_k \mid) - \mathrm{tr}(\Sigma^{-1})\Sigma_S, \tag{13a}$$

where

$$\Sigma_S = \frac{1}{N}\sum_{i=1}^{N} \vec{x}(\lambda_i)\vec{x}(\lambda_i)^{\dagger}. \tag{13b}$$

Anderson [1963] calculated $\hat{\Theta}$ that maximizes the log-likelihood function,

$$\mathcal{L}(\hat{\Theta}) = \log \left(\frac{\prod_{i=k+1}^{p} l_i^{\frac{1}{p-k}}}{\frac{1}{p-k}\sum_{i=k+1}^{p} l_i} \right)^{(p-k)N}, \tag{14}$$

where l_i are the eigenvalues of Σ_S and $l_1 > l_2 \cdots > l_p$

The number of free parameters for Θ_k are $k(2p-k)$, so the criterion for this problem is given by

$$AIC(k) = \log \left(\frac{\prod_{i=k+1}^{p} l_i^{\frac{1}{p-k}}}{\frac{1}{p-k}\sum_{i=k+1}^{p} l_i} \right)^{(p-k)N} + 2k(2p-k) \tag{15}$$

A minimum in equation 15, will give us the number of independent signals (k) needed to model the data. The first term of AIC can be understood as a measurement of the likeness of our model to reproduce the data against the second term that accounts for the number of parameters to be used. When applied to the entire cube of data AIC gives a minimum at $k = 15$, i.e. we need only the first 15 principal components.

References

B. Acke and M. E. van den Ancker. ISO spectroscopy of disks around Herbig Ae/Be stars. *A&A*, 426:151--170, October 2004. doi: 10.1051/0004-6361:20040400. 29

H. Akaike. A New Look at the Statistical Model Identification. *IEEE Transactions on Automatic Control*, 19:716--723, 1974. 18

J. M. Alcala, E. Covino, M. Franchini, J. Krautter, L. Terranegra, and R. Wichmann. T-Chamaeleontis - a Weak-Line Yy-Orionis Star. *A&A*, 272:225, May 1993. 30

A. Amara and S. P. Quanz. PYNPOINT: an image processing package for finding exoplanets. *Monthly Notices of the Royal Astronomical Society*, 427:948--955, December 2012. doi: 10.1111/j.1365-2966.2012.21918.x. 1, 8, 16, 18, 20, 49

T. W. Anderson. Asymptotic Theory for Principal Component Analysis. *The Annals of Mathematical Statistics*, 34(1):122--148, 1963. doi: 10.2307/2991288. URL http://dx.doi.org/10.2307/2991288. 53

M. Benisty, E. Tatulli, F. Ménard, and M. R. Swain. The complex structure of the disk around HD 100546. The inner few astronomical units. *A&A*, 511:A75, February 2010. doi: 10.1051/0004-6361/200913590. 29, 43

J.-L. Beuzit, M. Feldt, K. Dohlen, D. Mouillet, P. Puget, J. Antichi, P. Baudoz, A. Boccaletti, M. Carbillet, J. Charton, R. Claudi, T. Fusco, R. Gratton, T. Henning, N. Hubin, F. Joos, M. Kasper, M. Langlois, C. Moutou, J. Pragt, P. Rabou, M. Saisse, H. M. Schmid, M. Turatto, S. Udry, F. Vakili, R. Waters, and F. Wildi. SPHERE: A Planet Finder Instrument for the VLT. In *In the Spirit of Bernard Lyot: The Direct Detection of Planets and Circumstellar Disks in the 21st Century*, June 2007. 5

B. Biller, S. Lacour, A. Juhász, M. Benisty, G. Chauvin, J. Olofsson, J.-U. Pott, A. Müller, A. Sicilia-Aguilar, M. Bonnefoy, P. Tuthill, P. Thebault, T. Henning, and A. Crida. A Likely Close-in Low-mass Stellar Companion to the Transitional Disk Star HD 142527. *The Astrophysical Journal Letters*, 753:L38, July 2012. doi: 10.1088/2041-8205/753/2/L38. 5, 29

B. A. Biller, L. M. Close, E. Masciadri, R. Lenzen, W. Brandner, D. McCarthy, T. Henning, E. L. Nielsen, M. Hartung, S. Kellner, K. Geissler, and M. Kasper. Contrast limits with the Simultaneous Differential Extrasolar Planet Imager (SDI) at the VLT and MMT. In *Society of Photo-Optical Instrumentation Engineers (SPIE) Conference Series*, volume 6272 of *Society of Photo-Optical Instrumentation Engineers (SPIE) Conference Series*, July 2006. doi: 10.1117/12.671771. 8

H. Bonnet, R. Abuter, A. Baker, W. Bornemann, A. Brown, R. Castillo, R. Conzelmann, R. Damster, R. Davies, B. Delabre, R. Donaldson, C. Dumas, F. Eisenhauer, E. Elswijk, E. Fedrigo, G. Finger, H. Gemperlein, R. Genzel, A. Gilbert, G. Gillet, A. Goldbrunner, M. Horrobin, R. Ter Horst, S. Huber, N. Hubin, C. Iserlohe, A. Kaufer, M. Kissler-Patig, J. Kragt, G. Kroes, M. Lehnert, W. Lieb, J. Liske, J.-L. Lizon, D. Lutz, A. Modigliani, G. Monnet, N. Nesvadba, J. Patig, J. Pragt, J. Reunanen, C. Röhrle, S. Rossi, R. Schmutzer, T. Schoenmaker, J. Schreiber, S. Stroebele, T. Szeifert, L. Tacconi, M. Tecza, N. Thatte, S. Tordo, P. van der Werf, and H. Weisz. First light of SINFONI at the VLT. *The Messenger*, 117:17--24, September 2004. 2

J. Bouwman, A. de Koter, C. Dominik, and L. B. F. M. Waters. The origin of crystalline silicates in the Herbig Be star HD 100546 and in comet Hale-Bopp. *A&A*, 401:577--592, April 2003. doi: 10.1051/0004-6361:20030043. 29

G. Bryden, X. Chen, D. N. C. Lin, R. P. Nelson, and J. C. B. Papaloizou. Tidally Induced Gap Formation in Protostellar Disks: Gap Clearing and Suppression of Protoplanetary Growth. *The Astrophysical Journal*, 514:344--367, March 1999. doi: 10.1086/306917. 40

H. Canovas, F. Ménard, A. Hales, A. Jordán, M. R. Schreiber, S. Casassus, T. M. Gledhill, and C. Pinte. Near-infrared imaging polarimetry of HD 142527. *A&A*, 556:A123, August 2013. doi: 10.1051/0004-6361/201321924. viii, 7, 32, 36, 40

S. Casassus, S. Perez M., A. Jordán, F. Ménard, J. Cuadra, M. R. Schreiber, A. S. Hales, and B. Ercolano. The Dynamically Disrupted Gap in HD 142527. *The Astrophysical Journal Letters*, 754:L31, August 2012. doi: 10.1088/2041-8205/754/2/L31. viii, 29, 36, 40

S. Casassus, G. van der Plas, S. P. M, W. R. F. Dent, E. Fomalont, J. Hagelberg, A. Hales, A. Jordán, D. Mawet, F. Ménard, A. Wootten, D. Wilner, A. M. Hughes, M. R. Schreiber, J. H. Girard, B. Ercolano, H. Canovas, P. E. Román, and V. Salinas. Flows of gas through a protoplanetary gap. *Monthly Notices of the Royal Astronomical Society*, 493:191--194, January 2013. doi: 10.1038/nature11769. 29, 32

L. da Silva, C. A. O. Torres, R. de La Reza, G. R. Quast, C. H. F. Melo, and M. F. Sterzik. Search for associations containing young stars (SACY). III. Ages and Li abundances. *A&A*, 508: 833--839, December 2009. doi: 10.1051/0004-6361/200911736. 30

P. T. de Zeeuw, R. Hoogerwerf, J. H. J. de Bruijne, A. G. A. Brown, and A. Blaauw. A HIPPARCOS Census of the Nearby OB Associations. *The Astronomical Journal*, 117:354--399, January 1999. doi: 10.1086/300682. 29

R. Dekany, A. Bouchez, M. Britton, V. Velur, M. Troy, J. C. Shelton, and J. Roberts. PALM-3000: visible light AO on the 5.1-meter Telescope. In *Society of Photo-Optical Instrumentation Engineers (SPIE) Conference Series*, volume 6272 of *Society of Photo-Optical Instrumentation Engineers (SPIE) Conference Series*, July 2006. doi: 10.1117/12.674496. 5

F. Eisenhauer, R. Abuter, K. Bickert, F. Biancat-Marchet, H. Bonnet, J. Brynnel, R. D. Conzelmann, B. Delabre, R. Donaldson, J. Farinato, E. Fedrigo, R. Genzel, N. N. Hubin, C. Iserlohe, M. E. Kasper, M. Kissler-Patig, G. J. Monnet, C. Roehrle, J. Schreiber, S. Stroebele, M. Tecza,

N. A. Thatte, and H. Weisz. SINFONI - Integral field spectroscopy at 50 milli-arcsecond resolution with the ESO VLT. In M. Iye and A. F. M. Moorwood, editors, *Society of Photo-Optical Instrumentation Engineers (SPIE) Conference Series*, volume 4841 of *Society of Photo-Optical Instrumentation Engineers (SPIE) Conference Series*, pages 1548--1561, March 2003. doi: 10.1117/12.459468. 2

C. Espaillat, P. D'Alessio, J. Hernández, E. Nagel, K. L. Luhman, D. M. Watson, N. Calvet, J. Muzerolle, and M. McClure. Unveiling the Structure of Pre-transitional Disks. *The Astrophysical Journal*, 717:441--457, July 2010. doi: 10.1088/0004-637X/717/1/441. 30

B. Flury and H. Riedwyl. *Multivariate Statistics: A Practical Approach*. C R C Press LLC, 1988. 39

K. B. Follette, M. Tamura, J. Hashimoto, B. Whitney, C. Grady, L. Close, S. M. Andrews, J. Kwon, J. Wisniewski, T. D. Brandt, S. Mayama, R. Kandori, R. Dong, L. Abe, W. Brandner, J. Carson, T. Currie, S. E. Egner, M. Feldt, M. Goto, O. Guyon, Y. Hayano, M. Hayashi, S. Hayashi, T. Henning, K. Hodapp, M. Ishii, M. Iye, M. Janson, G. R. Knapp, T. Kudo, N. Kusakabe, M. Kuzuhara, M. W. McElwain, T. Matsuo, S. Miyama, J.-I. Morino, A. Moro-Martin, T. Nishimura, T.-S. Pyo, E. Serabyn, H. Suto, R. Suzuki, M. Takami, N. Takato, H. Terada, C. Thalmann, D. Tomono, E. L. Turner, M. Watanabe, T. Yamada, H. Takami, and T. Usuda. Mapping H-band Scattered Light Emission in the Mysterious SR21 Transitional Disk. *The Astrophysical Journal*, 767:10, April 2013. doi: 10.1088/0004-637X/767/1/10. 7

H. Fujiwara, M. Honda, H. Kataza, T. Yamashita, T. Onaka, M. Fukagawa, Y. K. Okamoto, T. Miyata, S. Sako, T. Fujiyoshi, and I. Sakon. The Asymmetric Thermal Emission of the Protoplanetary Disk Surrounding HD 142527 Seen by Subaru/COMICS. *The Astrophysical Journal Letters*, 644:L133--L136, June 2006. doi: 10.1086/505597. 40

M. Fukagawa, M. Tamura, Y. Itoh, T. Kudo, Y. Imaeda, Y. Oasa, S. S. Hayashi, and M. Hayashi. Near-Infrared Images of Protoplanetary Disk Surrounding HD 142527. *The Astrophysical Journal Letters*, 636:L153--L156, January 2006. doi: 10.1086/500128. 29, 32, 40

O. Guyon, E. A. Pluzhnik, M. J. Kuchner, B. Collins, and S. T. Ridgway. Theoretical Limits on Extrasolar Terrestrial Planet Detection with Coronagraphs. *The Astrophysical Journal Supplement Series*, 167:81--99, November 2006. doi: 10.1086/507630. 5

T. Henning, A. Burkert, R. Launhardt, C. Leinert, and B. Stecklum. Infrared imaging and millimetre continuum mapping of Herbig Ae/Be and FU Orionis stars. *A&A*, 336:565--586, August 1998. 29

S. Hinkley, B. R. Oppenheimer, R. Soummer, A. Sivaramakrishnan, L. C. Roberts, Jr., J. Kuhn, R. B. Makidon, M. D. Perrin, J. P. Lloyd, K. Kratter, and D. Brenner. Temporal Evolution of Coronagraphic Dynamic Range and Constraints on Companions to Vega. *The Astrophysical Journal*, 654:633--640, January 2007. doi: 10.1086/509063. vii, 4

N. Houk. *Michigan catalogue of two-dimensional spectral types for the HD stars*. 1978. 29

N. Huélamo, S. Lacour, P. Tuthill, M. Ireland, A. Kraus, and G. Chauvin. A companion candidate in the gap of the T Chamaeleontis transitional disk. *A&A*, 528:L7, April 2011. doi: 10.1051/0004-6361/201016395. 5, 30, 37

I.T. Jolliffe. *Principal Component Analysis,Second Edition*. Springer, 2002. 48

Hans-Peter Kriegel, Peer Kroger, Erich Schubert, and Arthur Zimek. A general framework for increasing the robustness of pca-based correlation clustering algorithms. In *IN: PROC. SSDBM*, 2008. 48

J. R. Kuhn, D. Potter, and B. Parise. Imaging Polarimetric Observations of a New Circumstellar Disk System. *The Astrophysical Journal Letters*, 553:L189--L191, June 2001. doi: 10.1086/320686. 7

D. Lafrenière, C. Marois, R. Doyon, D. Nadeau, and É. Artigau. A New Algorithm for Point-Spread Function Subtraction in High-Contrast Imaging: A Demonstration with Angular Differential Imaging. *The Astrophysical Journal*, 660:770--780, May 2007. doi: 10.1086/513180. 1, 8, 19

C. Leinert, R. van Boekel, L. B. F. M. Waters, O. Chesneau, F. Malbet, R. Köhler, W. Jaffe, T. Ratzka, A. Dutrey, T. Preibisch, U. Graser, E. Bakker, G. Chagnon, W. D. Cotton, C. Dominik, C. P. Dullemond, A. W. Glazenborg-Kluttig, A. Glindemann, T. Henning, K.-H. Hofmann, J. de Jong, R. Lenzen, S. Ligori, B. Lopez, J. Meisner, S. Morel, F. Paresce, J.-W. Pel, I. Percheron, G. Perrin, F. Przygodda, A. Richichi, M. Schöller, P. Schuller, B. Stecklum, M. E. van den Ancker, O. von der Lühe, and G. Weigelt. Mid-infrared sizes of circumstellar disks around Herbig Ae/Be stars measured with MIDI on the VLTI. *A&A*, 423:537--548, August 2004. doi: 10.1051/0004-6361:20047178. 29

R. Lenzen, L. Close, W. Brandner, B. Biller, and M. Hartung. A novel simultaneous differential imager for the direct imaging of giant planets. In A. F. M. Moorwood and M. Iye, editors, *Society of Photo-Optical Instrumentation Engineers (SPIE) Conference Series*, volume 5492 of *Society of Photo-Optical Instrumentation Engineers (SPIE) Conference Series*, pages 970--977, September 2004. doi: 10.1117/12.549406. 1

W. M. Liu, P. M. Hinz, M. R. Meyer, E. E. Mamajek, W. F. Hoffmann, and J. L. Hora. A Resolved Circumstellar Disk around the Herbig Ae Star HD 100546 in the Thermal Infrared. *The Astrophysical Journal Letters*, 598:L111--L114, December 2003. doi: 10.1086/380827. 29

B. Macintosh, M. Troy, R. Doyon, J. Graham, K. Baker, B. Bauman, C. Marois, D. Palmer, D. Phillion, L. Poyneer, I. Crossfield, P. Dumont, B. M. Levine, M. Shao, G. Serabyn, C. Shelton, G. Vasisht, J. K. Wallace, J.-F. Lavigne, P. Valee, N. Rowlands, K. Tam, and D. Hackett. Extreme adaptive optics for the Thirty Meter Telescope. In *Society of Photo-Optical Instrumentation Engineers (SPIE) Conference Series*, volume 6272 of *Society of Photo-Optical Instrumentation Engineers (SPIE) Conference Series*, July 2006. doi: 10.1117/12.672032. 15

C. Marois, R. Doyon, D. Nadeau, R. Racine, M. Riopel, P. Vallée, and D. Lafrenière. TRIDENT: An Infrared Differential Imaging Camera Optimized for the Detection of Methanated Substellar Companions. *Publications of the Astronomical Society of the Pacific*, 117:745--756, July 2005. doi: 10.1086/431347. 1, 7, 8

C. Marois, D. Lafrenière, R. Doyon, B. Macintosh, and D. Nadeau. Angular Differential Imaging: A Powerful High-Contrast Imaging Technique. *The Astrophysical Journal*, 641:556--564, April 2006. doi: 10.1086/500401. 1, 8

D. Mawet, L. Pueyo, P. Lawson, L. Mugnier, W. Traub, A. Boccaletti, J. T. Trauger, S. Gladysz, E. Serabyn, J. Milli, R. Belikov, M. Kasper, P. Baudoz, B. Macintosh, C. Marois, B. Oppenheimer, H. Barrett, J.-L. Beuzit, N. Devaney, J. Girard, O. Guyon, J. Krist, B. Mennesson, D. Mouillet, N. Murakami, L. Poyneer, D. Savransky, C. Vérinaud, and J. K. Wallace. Review of small-angle coronagraphic techniques in the wake of ground-based second-generation adaptive optics systems. In *Society of Photo-Optical Instrumentation Engineers (SPIE) Conference Series*, volume 8442 of *Society of Photo-Optical Instrumentation Engineers (SPIE) Conference Series*, September 2012. doi: 10.1117/12.927245. 7

M. Mayor and D. Queloz. A Jupiter-mass companion to a solar-type star. *Monthly Notices of the Royal Astronomical Society*, 378:355--359, November 1995. doi: 10.1038/378355a0. 1

N. Ohashi. Observational signature of planet formation: The ALMA view. *Astrophysics and Space Science*, 313:101--107, January 2008. doi: 10.1007/s10509-007-9667-5. 40

J. Olofsson, M. Benisty, J.-C. Augereau, C. Pinte, F. Ménard, E. Tatulli, J.-P. Berger, F. Malbet, B. Merín, E. F. van Dishoeck, S. Lacour, K. M. Pontoppidan, J.-L. Monin, J. M. Brown, and G. A. Blake. Warm dust resolved in the cold disk around T Chamaeleontis with VLTI/AMBER. *A&A*, 528:L6, April 2011. doi: 10.1051/0004-6361/201016074. 30

B. R. Oppenheimer and S. Hinkley. High-Contrast Observations in Optical and Infrared Astronomy. *Annual Review of Astronomy and Astrophysics*, 47:253--289, September 2009. doi: 10.1146/annurev-astro-082708-101717. vii, 1, 3, 6, 7

B. R. Oppenheimer, D. Brenner, S. Hinkley, N. Zimmerman, A. Sivaramakrishnan, R. Soummer, J. Kuhn, J. R. Graham, M. Perrin, J. P. Lloyd, L. C. Roberts, Jr., and D. M. Harrington. The Solar-System-Scale Disk around AB Aurigae. *The Astrophysical Journal*, 679:1574--1581, June 2008. doi: 10.1086/587778. 7

B. R. Oppenheimer, C. Baranec, C. Beichman, D. Brenner, R. Burruss, E. Cady, J. R. Crepp, R. Dekany, R. Fergus, D. Hale, L. Hillenbrand, S. Hinkley, D. W. Hogg, D. King, E. R. Ligon, T. Lockhart, R. Nilsson, I. R. Parry, L. Pueyo, E. Rice, J. E. Roberts, L. C. Roberts, Jr., M. Shao, A. Sivaramakrishnan, R. Soummer, T. Truong, G. Vasisht, A. Veicht, F. Vescelus, J. K. Wallace, C. Zhai, and N. Zimmerman. Reconnaissance of the HR 8799 Exosolar System. I. Near-infrared Spectroscopy. *The Astrophysical Journal*, 768:24, May 2013. doi: 10.1088/0004-637X/768/1/24. 43

O. Panić, E. F. van Dishoeck, M. R. Hogerheijde, A. Belloche, R. Güsten, W. Boland, and A. Baryshev. Observations of warm molecular gas and kinematics in the disc around HD 100546. *A&A*, 519:A110, September 2010. doi: 10.1051/0004-6361/200913709. 29

E. Pantin, C. Waelkens, and P. O. Lagage. ADONIS observations of the HD 100546 circumstellar dust disk. *A&A*, 361:L9--L12, September 2000. 29

M. D. Perrin, J. R. Graham, P. Kalas, J. P. Lloyd, C. E. Max, D. T. Gavel, D. M. Pennington, and E. L. Gates. Laser guide star adaptive optics imaging polarimetry of Herbig Ae/Be stars. In D. Bonaccini Calia, B. L. Ellerbroek, and R. Ragazzoni, editors, *Society of Photo-Optical Instrumentation Engineers (SPIE) Conference Series*, volume 5490 of *Society of Photo-Optical Instrumentation Engineers (SPIE) Conference Series*, pages 309--320, October 2004. doi: 10.1117/12.551932. 7

L. Pueyo, J. R. Crepp, G. Vasisht, D. Brenner, B. R. Oppenheimer, N. Zimmerman, S. Hinkley, I. Parry, C. Beichman, L. Hillenbrand, L. C. Roberts, R. Dekany, M. Shao, R. Burruss, A. Bouchez, J. Roberts, and R. Soummer. Application of a Damped Locally Optimized Combination of Images Method to the Spectral Characterization of Faint Companions Using an Integral Field Spectrograph. *The Astrophysical Journal Supplement Series*, 199:6, March 2012a. doi: 10.1088/0067-0049/199/1/6. 1, 9, 20

L. Pueyo, L. Hillenbrand, G. Vasisht, B. R. Oppenheimer, J. D. Monnier, S. Hinkley, J. Crepp, L. C. Roberts, Jr., D. Brenner, N. Zimmerman, I. Parry, C. Beichman, R. Dekany, M. Shao, R. Burruss, E. Cady, J. Roberts, and R. Soummer. Constraining Mass Ratio and Extinction in the FU Orionis Binary System with Infrared Integral Field Spectroscopy. *The Astrophysical Journal*, 757:57, September 2012b. doi: 10.1088/0004-637X/757/1/57. 1, 15

S. P. Quanz, A. Amara, M. R. Meyer, M. A. Kenworthy, M. Kasper, and J. H. Girard. A Young Protoplanet Candidate Embedded in the Circumstellar Disk of HD 100546. *The Astrophysical Journal Letters*, 766:L1, March 2013a. doi: 10.1088/2041-8205/766/1/L1. 37

S. P. Quanz, A. Amara, M. R. Meyer, M. A. Kenworthy, M. Kasper, and J. H. Girard. A Young Protoplanet Candidate Embedded in the Circumstellar Disk of HD 100546. *The Astrophysical Journal Letters*, 766:L1, March 2013b. doi: 10.1088/2041-8205/766/1/L1. 29

R. Racine, G. A. H. Walker, D. Nadeau, R. Doyon, and C. Marois. Speckle Noise and the Detection of Faint Companions. *Publications of the Astronomical Society of the Pacific*, 111:587--594, May 1999. doi: 10.1086/316367. 4, 8

J. Rameau, G. Chauvin, A.-M. Lagrange, P. Thébault, J. Milli, J. H. Girard, and M. Bonnefoy. High-contrast imaging of the close environment of HD 142527. VLT/NaCo adaptive optics thermal and angular differential imaging. *A&A*, 546:A24, October 2012. doi: 10.1051/0004-6361/201219736. 40

J. Rissanen. Modeling by shortest data description. *Automatica*, 14(5):465--471, September 1978. ISSN 00051098. doi: 10.1016/0005-1098(78)90005-5. URL http://dx.doi.org/10.1016/0005-1098(78)90005-5. 18

M. Rodenhuis, H. Canovas, S. V. Jeffers, M. de Juan Ovelar, M. Min, L. Homs, and C. U. Keller. The extreme polarimeter: design, performance, first results and upgrades. In *Society of Photo-Optical Instrumentation Engineers (SPIE) Conference Series*, volume 8446 of *Society of Photo-Optical Instrumentation Engineers (SPIE) Conference Series*, September 2012. doi: 10.1117/12.927203. 7

J. Schneider, P. Le Sidaner, R. Savalle, and I. Zolotukhin. The exoplanet.eu Database and Associated VO Services. In P. Ballester, D. Egret, and N. P. F. Lorente, editors, *Astronomical Data Analysis Software and Systems XXI*, volume 461 of *Astronomical Society of the Pacific Conference Series*, page 447, September 2012. 1

Gideon Schwarz. Estimating the Dimension of a Model. *The Annals of Statistics*, 6(2):461--464, 1978. ISSN 00905364. doi: 10.2307/2958889. URL http://dx.doi.org/10.2307/2958889. 18

R. Soummer, A. Ferrari, C. Aime, and L. Jolissaint. Speckle Noise and Dynamic Range in Coronagraphic Images. *The Astrophysical Journal*, 669:642--656, November 2007. doi: 10.1086/520913. 4

R. Soummer, L. Pueyo, and J. Larkin. Detection and Characterization of Exoplanets and Disks Using Projections on Karhunen-Loève Eigenimages. *The Astrophysical Journal Letters*, 755: L28, August 2012. doi: 10.1088/2041-8205/755/2/L28. 1, 8, 16, 18

W. B. Sparks and H. C. Ford. Imaging Spectroscopy for Extrasolar Planet Detection. *The Astrophysical Journal*, 578:543--564, October 2002. doi: 10.1086/342401. 1, 8, 9, 15, 16, 18

K. R. Stapelfeldt. Extrasolar planets and star formation: science opportunities for future ELTs. In P. Whitelock, M. Dennefeld, and B. Leibundgut, editors, *The Scientific Requirements for Extremely Large Telescopes*, volume 232 of *IAU Symposium*, pages 149--158, 2006. doi: 10.1017/S1743921306000408. 4

E. Tatulli, M. Benisty, F. Ménard, P. Varnière, C. Martin-Zaïdi, W.-F. Thi, C. Pinte, F. Massi, G. Weigelt, K.-H. Hofmann, and R. G. Petrov. Constraining the structure of the planet-forming region in the disk of the Herbig Be star HD 100546. *A&A*, 531:A1, July 2011. doi: 10.1051/0004-6361/201016165. 29

N. Thatte, R. Abuter, M. Tecza, E. L. Nielsen, F. J. Clarke, and L. M. Close. Very high contrast integral field spectroscopy of AB Doradus C: 9-mag contrast at 0.2arcsec without a coronagraph using spectral deconvolution†. *Monthly Notices of the Royal Astronomical Society*, 378:1229--1236, July 2007. doi: 10.1111/j.1365-2966.2007.11717.x. vii, 1, 12, 16, 17, 19

C. A. O. Torres, G. R. Quast, C. H. F. Melo, and M. F. Sterzik. *Young Nearby Loose Associations*, page 757. December 2008. 30

M. E. van den Ancker, P. S. The, H. R. E. Tjin A Djie, C. Catala, D. de Winter, P. F. C. Blondel, and L. B. F. M. Waters. HIPPARCOS data on Herbig Ae/Be stars: an evolutionary scenario. *A&A*, 324:L33--L36, August 1997. 29

F. van Leeuwen. Validation of the new Hipparcos reduction. *A&A*, 474:653--664, November 2007. doi: 10.1051/0004-6361:20078357. 29

A. P. Verhoeff, M. Min, E. Pantin, L. B. F. M. Waters, A. G. G. M. Tielens, M. Honda, H. Fujiwara, J. Bouwman, R. van Boekel, S. M. Dougherty, A. de Koter, C. Dominik, and G. D. Mulders. The complex circumstellar environment of HD 142527. *A&A*, 528:A91, April 2011. doi: 10.1051/0004-6361/201014952. 29, 40

S. L. A. Vieira, M. A. Pogodin, and G. A. P. Franco. Spectroscopic study of the Herbig Be star HD 100546. *A&A*, 345:559--575, May 1999. 29

C. Waelkens, L. B. F. M. Waters, M. S. de Graauw, E. Huygen, K. Malfait, H. Plets, B. Vandenbussche, D. A. Beintema, D. R. Boxhoorn, H. J. Habing, A. M. Heras, D. J. M. Kester, F. Lahuis, P. W. Morris, P. R. Roelfsema, A. Salama, R. Siebenmorgen, N. R. Trams, N. R. van der Bliek, E. A. Valentijn, and P. R. Wesselius. SWS observations of young main-sequence stars with dusty circumstellar disks. *A&A*, 315:L245--L248, November 1996. 29

Mati Wax and Thomas Kailath. Detection of signals by information theoretic criteria. *IEEE Transactions on Acoustics, Speech and Signal Processing*, 33(2):387--392, April 1985. ISSN 0096-3518. 18, 51

J. T. Wright and B. S. Gaudi. *Exoplanet Detection Methods*, page 489. 2013. doi: 10.1007/978-94-007-5606-9_10. 7